Solar Phys
DOI 10.1007/s11207-007-0330-7

Modeling and Measuring the Flux Reconnected and Ejected by the Two-Ribbon Flare/CME Event on 7 November 2004

Dana Longcope · Colin Beveridge · Jiong Qiu · B. Ravindra · Graham Barnes · Sergio Dasso

Received: 6 October 2006 / Accepted: 12 March 2007

Abstract Observations of the large two-ribbon flare on 7 November 2004 made using SOHO and TRACE data are interpreted in terms of a three-dimensional magnetic field model. Photospheric flux evolution indicates that -1.4×10^{43} Mx^2 of magnetic helicity was injected into the active region during the 40-hour buildup prior to the flare. The magnetic model places a lower bound of 8×10^{31} ergs on the energy stored by this motion. It predicts that 5×10^{21} Mx of flux would need to be reconnected during the flare to release the stored energy. This total reconnection compares favorably with the flux swept up by the flare ribbons, which we measure using high-time-cadence TRACE images in 1 600 Å. Reconnection in the model must occur in a specific sequence that would produce a twisted flux rope containing significantly less flux and helicity (10^{21} Mx and -3×10^{42} Mx^2, respectively) than the active region as a whole. The predicted flux compares favorably with values inferred from the magnetic cloud observed by *Wind*. This combined analysis yields the first quantitative picture of the flux processed through a two-ribbon flare and coronal mass ejection.

D. Longcope (✉) · C. Beveridge · J. Qiu · B. Ravindra
Department of Physics, Montana State University, Bozeman, MT 59717, USA
e-mail: dana@physics.montana.edu

G. Barnes
Colorado Research Associates Division, NorthWest Research Associates Inc., 3380 Mitchell Lane, Boulder, CO 80301, USA

S. Dasso
Instituto de Astronomía y Física del Espacio, IAFE, CC. 67 Suc. 28, 1428 Buenos Aires, Argentina

S. Dasso
Departamento de Física, Facultad de Ciencias Exactas y Naturales, Universidad de Buenos Aires, 1428 Buenos Aires, Argentina

1. Introduction

1.1. Two-Ribbon Flares

Perhaps the most accepted and thoroughly studied cases of magnetic reconnection in astrophysics are two-ribbon solar flares. Contributions from Carmichael (1964), Sturrock (1968), Hirayama (1974), and Kopp and Pneuman (1976) were ultimately combined into a single model known as the CSHKP two-ribbon flare, depicted in Figure 1a. In this model, oppositely directed vertical field lines (A), either open or closing at great height, reconnect across a current sheet (CS). This reconnection converts pairs of (effectively) open field lines into closed field lines (C) crossing low over a polarity inversion line (PIL). Energy deposited into the most recently reconnected field lines evaporates chromospheric material to produce flare ribbons (R). As the volume of closed field lines increases, the reconnection point (X) moves upward and the flare ribbons move outward. Along with each closed field line the reconnection also creates a U-shaped disconnected field line contributing to the plasmoid (P) or flux rope ejected by a coronal mass ejection (CME).

In spite of its long-recognized success at explaining qualitative features of two-ribbon flares, the CSHKP model has only recently found wide use in quantitative measurements. Forbes and Priest (1984) proposed a general method for measuring the flux reconnected across the current sheet. To make this measurement the curves from each Hα flare ribbon are mapped onto a magnetogram and the vertical magnetic flux swept up by them over time is integrated. This method was applied by Poletto and Kopp (1986) to quantify the reconnection rate in two-ribbon flares (29 July 1973 and 21 May 1980) whose configurations were deemed well approximated by the two-dimensional CSHKP model. A series of recent applications of this method (Fletcher *et al.*, 2001; Qiu *et al.*, 2002) has used data of higher resolution and time cadence to make the same kind of measurement for several other flares. These have yielded flux transfer rates ranging from 0.5 to 20 GV for various flares.

One of the more serious difficulties presented by the application of the CSHKP model to a broader range of quantitative measurements is the lack of an accepted three-dimensional generalization. In the cases just cited the researchers were therefore forced to interpret the

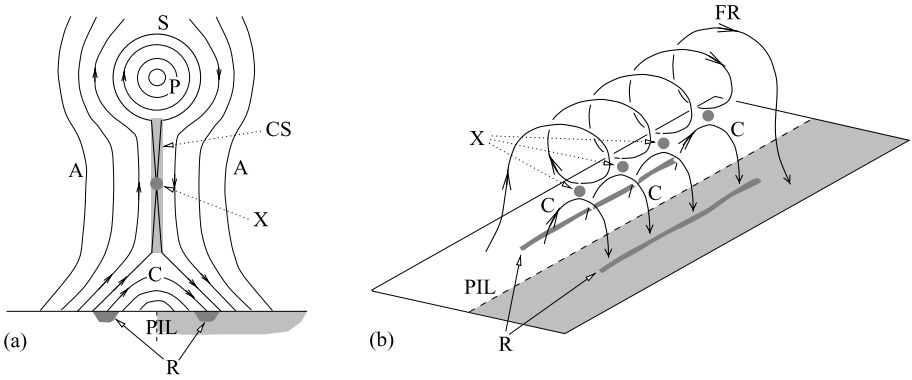

Figure 1 Basic elements of the CSHKP two-ribbon flare model in two (a) and three (b) dimensions. Open field lines (A) are separated by a current sheet (CS). They reconnect at a magnetic X-point (X) to create closed field lines (C) and a plasmoid (P). The energy released by reconnection creates chromospheric flare ribbons (R) on either side of the PIL, just inside the separatrix (S). In the three-dimensional version (b) reconnection occurs at several sites (X) to create closed field lines (C) and a twisted flux rope (FR) instead of the plasmoid.

observed flares as if they were two-dimensional. Reconnection is assumed to occur simultaneously along a line of magnetic X-points. The ribbons are the footpoints of the separatrices from these X-points and their motion, which maps the progress of the reconnection, is necessarily perpendicular. Each reconnection forges a single new closed field line and a disconnected field line at the same time. In this simple picture the flux swept up by the positive ribbon should exactly match that swept up by the negative ribbon.

It is hardly surprising that observations of actual two-ribbon flares fail to match the two-dimensional model in every detail. In many cases the fluxes calculated from each of the ribbons disagree by a significant amount (Fletcher *et al.*, 2001). More detailed images of the flare ribbons, made by TRACE in 1 600 Å, reveal them to consist of numerous small elements moving parallel rather than perpendicular to the overall ribbon axis (Fletcher, Pollock, and Potts, 2004). Hard X-ray footpoints, presumably produced by electrons precipitating from the reconnection site, generally do occur within the ribbon; but they occur at a single point, which also tends to move along the ribbon rather than perpendicular to it. It is not clear how these structures and motions are to be reconciled with the two-dimensional CSHKP model.

1.2. Coronal Mass Ejections

The CSHKP model also implies that a relation should exist between the flux reconnected in the flare and the flux ejected by the CME. This relation is not easy to glean from the two-dimensional model, which produces a strictly disconnected plasmoid. Maintaining the purely two-dimensional perspective one may distinguish between poloidal and toroidal flux, of which any reconnection will affect only the former. From this standpoint one expects the amount of photospheric reconnection to match the net *poloidal* flux in the ejecta and the toroidal flux in the ejecta to be arbitrary (being oriented along the ignorable direction).

It is possible to use *in situ* observation of CME ejecta, particularly high-energy electrons, to infer the actual connectivity of the heliospheric field lines (Feldman *et al.*, 1975). Such observations (Gosling *et al.*, 1987) show that, rather than disconnected plasmoids, a CME produces a twisted flux rope with two feet anchored back at the Sun even as its apex passes 1 AU. Explaining such flux ropes, and their often complex inter-mixture of open and closed field lines, has led to a more faithfully three-dimensional picture whereby CSHKP-like reconnection adds twist to a flux rope as it erupts (Gosling, 1990; Gosling, Birn, and Hesse, 1995). Cartoons of this reconnection scenario, as in Figure 1b, seem consistent with the observations, but they have not yet been converted into a quantitative model. It is clear from the cartoon that the lack of symmetry makes it impossible to distinguish in practice between toroidal and poloidal flux. There is not at this time a quantitative relationship predicted between the flux reconnected and that in the flux rope.

The structure and topology of ejected flux ropes have been best characterized in the class of events known as *magnetic clouds* (MCs). First identified by Burlaga *et al.* (1981), these are coherent structures in the solar wind characterized by low proton temperature and a strong, smoothly varying magnetic field. Assuming them to be twisted flux ropes in magnetic equilibrium, several authors have succeeded in matching the observations to a model equilibrium and thereby inferring global properties such as axis orientation, net flux, and helicity content (Lepping, Burlaga, and Jones, 1990; Hu and Sonnerup, 2002; Dasso *et al.*, 2003, 2005a).

Leamon *et al.* (2004) performed such fits to 12 MCs and found that their inferred axial fluxes roughly matched the flux of the entire active region (AR) whose CME had ejected it. This seems to support the idea that the flux rope is the result of ejection of flux from the AR.

Leamon *et al.* (2004) failed to find a simple relationship between the amount of twist in the flux rope and the helicity of the AR, suggesting a rather complex pattern of reconnection occurs during the eruption itself. However, in the interplanetary flux ropes the amount of the twist is a local quantity and it can depend strongly on the radial distance to the cloud center, with a typical value of $\sim$2 turns per AU near the cloud axis (Gulisano *et al.*, 2005), reaching a very large twist at their periphery, being infinity under the classical Lundquist's model (Lundquist, 1950). It follows that a proper comparison to make would be to the total helicity of the MC. Mandrini *et al.* (2005) and Luoni *et al.* (2005) compared, respectively, the helicity released from a very small AR and a very large AR with the helicity content of their interplanetary manifestation. They found a very good agreement in the helicity values (small AR with small MC, and large AR with large MC), finding a difference of $\sim$3 orders of magnitude between the smaller and the larger events, in both AR and MC (Dasso *et al.*, 2005b).

This work is an attempt to combine observations of a two-ribbon flare and a magnetic cloud into a coherent scenario of three-dimensional reconnection. Measurements of the magnetic fluxes in the AR, swept up by the flare ribbons, and in the MC can be compared to elucidate the inter-relation of these features. These measurements are made here for the two-ribbon flare from NOAA AR 10696, which occurred on 7 November 2004 at 16:15 UT. Using data from SOHO/MDI we construct a three-dimensional model of the pre-flare magnetic field during 40 hours of its evolution, following the preceding flare (6 November 00:11 UT). This model can be used to make quantitative predictions of the reconnection that would occur in the two-ribbon flare, the energy it would release, and the flux and magnetic helicity in the flux rope it would produce. Each of these predictions is then compared to observations. The reconnected flux is compared to the amount of photospheric flux swept up by the flare ribbons made using TRACE 1 600 Å data. The ejected flux and helicity are compared to values inferred by fitting the magnetic cloud observations made by the *Wind* spacecraft.

1.3. Three-Dimensional Reconnection

One of the challenges in reconciling the observations with a realistic model is to understand reconnection in three dimensions. There has been a recent series of theoretical investigations of three-dimensional reconnection at magnetic separators (Greene, 1988; Lau and Finn, 1990; Longcope, 2005; Démoulin, 2006), which are the topological analog in three dimensions of an X-point: They occur at the interface of four distinct types of field lines. While reconnection can be defined in myriad ways, the more subtle of which do not even require topological boundaries (Hesse and Schindler, 1988; Hornig and Schindler, 1996; Priest, Hornig, and Pontin, 2003), separator reconnection leads to instantaneous large-scale changes, providing the opportunity for remote observational identification and quantitative measurements (Longcope *et al.*, 2005).

To quantify the flux undergoing topological change in a flare we must adopt a method for observationally characterizing the connectivity of coronal field lines. The minimum current corona (MCC) model proposed by Longcope (1996) does this in a straightforward way by defining distinct source regions in the photosphere. Under the assumption that the amounts of flux linking pairs of source regions, called the *domain fluxes*, remain fixed prior to reconnection the MCC model is able to quantify the pre-flare energy storage. Within this framework reconnection is simply the transport of flux between domains, similar to the creation of new closed (C) and plasmoid (P) flux in the CSHKP model (Figure 1). In the MCC model this must occur at a separator just as it occurs at an X-point in the CSHKP model.

The following section describes the topological model of the pre-flare magnetic field. Magnetogram data from SOHO/MDI are used to generate a quantitative model of the helicity injected and the energy stored prior to the flare. The subsequent section presents observation of the flare ribbons in 1 600 Å and the measurement of the reconnected flux. The corresponding value is obtained from the model. Section 4 then presents the reconnection sequence predicted by the model: a quantitative version of the Gosling (1990) picture. *Wind* data of a related MC are then analyzed to determine the flux and helicity ejected during the flare. These measurements are compared to the model prediction. The final section discusses the overall understanding of two-ribbon flares and CMEs that emerges from the quantitative agreement between the magnetic model and the observations.

2. The Topological Model: MCC

2.1. Partitioning the Magnetograms

All of our photospheric flux measurements use full-disk magnetograms from SOI/MDI (Scherrer *et al.*, 1995). Five successive magnetograms one-minute apart are averaged together to form a single low-noise magnetogram. Following the cross-calibration study of Berger and Lites (2003) we multiply the reported line-of-sight magnetic field values by 1.56. We make the further assumption that the field is approximately radial at the photosphere and therefore divide the line-of-sight component by the cosine of the angle from disk center to derive a radial field B_z at each pixel. A sequence of three M-class flares (M9.3, M5.9, and M3.6) occurs within the first two hours of 6 November 2004 (00:11 UT, 00:44 UT, and 01:40 UT). We take this as our starting point and form an hourly sequence of low-noise magnetograms beginning at 00:03 UT on 6 November. We use a sequence ending at 16:03 UT on 7 November as the buildup leading to the X2 flare at 16:06 UT.

To estimate the amount of flux topologically changed (*i.e.*, reconnected) during the X2 flare, we divide the photospheric field into a set of unipolar regions, called *source regions*. The process for defining regions is called partitioning and is detailed in Barnes, Longcope, and Leka (2005) and Longcope, Ravindra, and Barnes (2007). The first step is to derive a local correlation tracking (LCT) velocity from successive pairs of magnetograms (November and Simon, 1988). This is done using a Gaussian apodizing window $7''$ wide, applied only to pixels with field strength exceeding 50 G.

The basic step in partitioning is to group pixels exceeding a threshold, $B_{\rm thr} = 35$ G, downhill from a local maximum into a region. Some of the boundaries between these regions will originate in saddle points of the function $B_z(x, y)$. Next, in a step called saddle-merging, we combine regions by eliminating any boundary whose saddle point is less than 300 G below either maximum it separates. Finally, we discard any region with less than 7.6×10^{19} Mx of net flux on the premise that it is too small to contribute significant energy to the active region field. Each acceptable region is then assigned a unique label. To maintain continuity of region labels we generate a reference by advecting the previous partition to the present time using the LCT velocity, and we assign a region the label of the reference region with which it overlaps most (it is given a new label in the case of the first partitioning or when it overlaps no reference regions). We have found that performing the partitioning in reverse chronological order provides the most stable result (Longcope, Ravindra, and Barnes, 2007). When propagating regions backward a fragmentation appears as a merging and the fragments are assigned separate labels that are then combined into the single progenitor.

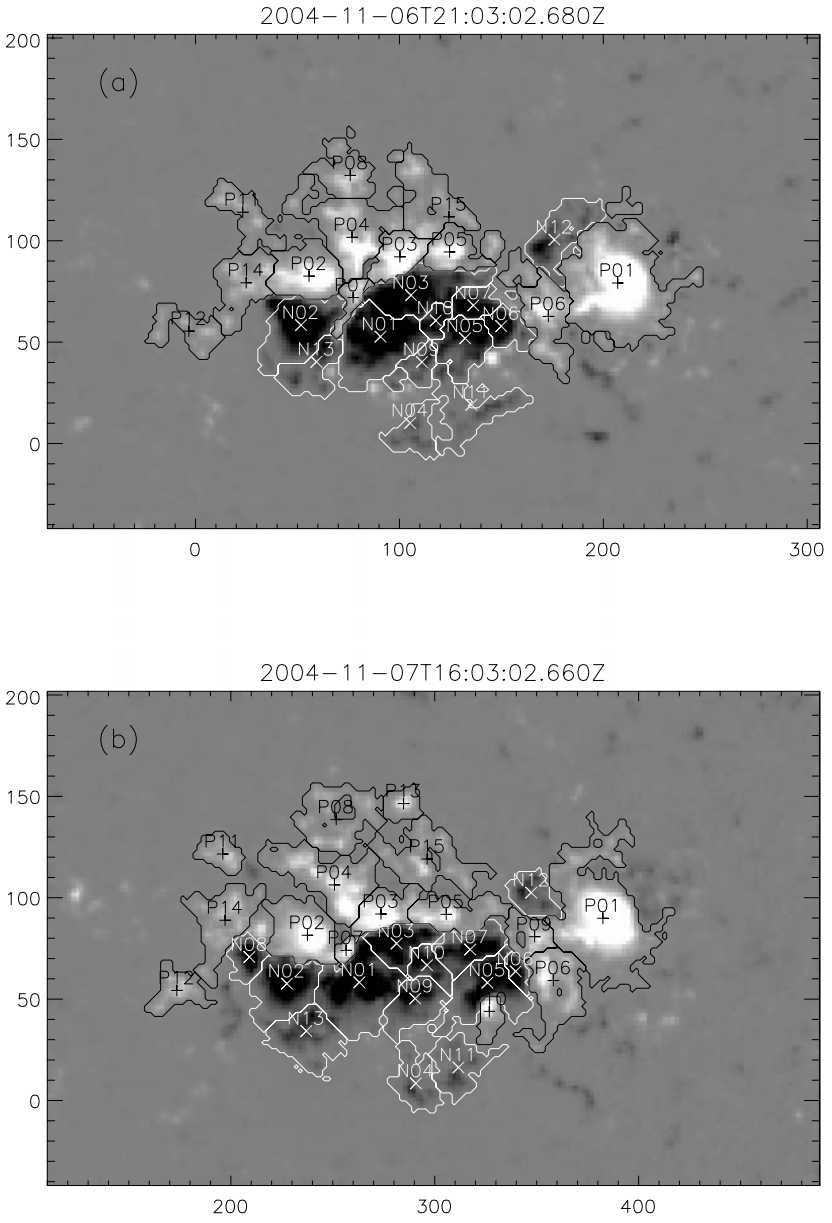

Figure 2 The partition of AR 10696 at two times during its evolution. The gray scale shows the radial magnetic field $B_z(x, y)$ scaled from −1 000 to 1 000 G. The regions are outlined and the centroids are denoted by + and × symbols. (a) From 6 November 21:03 UT and (b) from 7 November 16:03 (just before the X2 flare).

We perform the partitioning on the hourly sequence of averaged magnetograms, beginning 6 November 00:03 UT and ending 7 November 16:03 UT. The result is a set of evolving unipolar regions that includes all of the strongest flux; examples are shown in Figure 2.

A region $\mathcal{R}_a$ is characterized by its net flux and its centroid,

$$\Phi_a = \int_{\mathcal{R}_a} B_z(x, y)\,\mathrm{d}x\,\mathrm{d}y, \tag{1}$$

$$\bar{\mathbf{x}}_a = \frac{1}{\Phi_a}\int_{\mathcal{R}_a} \mathbf{x} B_z(x, y)\,\mathrm{d}x\,\mathrm{d}y. \tag{2}$$

According to the summary of the partition of 7 November 16:03 UT, shown in Figure 3a, approximately 85% of the flux in each polarity is assigned to one of 28 different regions. This is a much larger fraction of those pixels with $|B_z| > 35$ G, but it is still less than 100%, owing to the discard of small regions, mostly outside the main AR. The largest region, P01, has net flux 6.8×10^{21} Mx at this time and its flux varies little over the 40-hour sequence. The cumulative histograms shown in Figure 3b form a characteristic Υ-pattern, indicating that the majority of flux is assigned to a handful of the largest regions. These are the concentrations, including sunspots, whose interaction presumably sets the stage for the large energy releases observed.

The line-of-sight magnetograms of MDI are known to be less sensitive to fields stronger than approximately 1 700 G (Berger and Lites, 2003). After multiplying by the calibration factor of 1.56, we find that our magnetograms contain some flux above that level. The histogram for 7 November at 16:03 UT (Figure 3a) shows flux above 1 700 G amounting to 5.8×10^{20} Mx in the positive regions and 3.0×10^{20} Mx in negative regions. These values, from integration of $|B_z| - 1\,700$ over those areas, provides an estimate of the inaccuracies from strong-field insensitivity (Longcope *et al.*, 2005). If all of the strong positive field fell in P01, that region's flux would be underestimated by no more than 8%, and the error in region N01 would be no more than 5% (Longcope *et al.*, 2005). We use these estimates of rather modest inaccuracies in total fluxes from strong-field insensitivity to justify our lack of special treatment of the strong field.

The present partitions exhibit so little variation in flux that we conclude that no significant emergence or submergence occurs over the 40-hour interval. This fact motivates us to simplify later analysis by constructing a *reduced* model in which all fluxes are held strictly constant. To optimize agreement around the time of the flare we fix the flux of each region to its value at 7 November 16:03 UT. We then reduce the centroiding noise (Barnes, Longcope, and Leka, 2005) by smoothing the trajectory $\bar{\mathbf{x}}_a(t)$ using a five-hour box-car filter. The resulting set of fluxes and evolving centroids constitutes our reduced model.

The overall evolution of the active region can be characterized by the flux of relative helicity into the corona. This can be calculated from the LCT velocity (Berger and Field, 1984; Chae, 2001; Démoulin and Berger, 2003) from the integral

$$\dot{H} = -2\int (\mathbf{v}\cdot\mathbf{A}_\mathrm{P}) B_z\,\mathrm{d}x\,\mathrm{d}y, \tag{3}$$

over the magnetogram, where $\mathbf{A}_\mathrm{P}$ is the vector potential field for the curl-free (potential) magnetic field matching $B_z(x, y)$. The motions of the centroids alone contribute a *braiding helicity* flux (Berger, 1984; Welsch and Longcope, 2003; Longcope, Ravindra, and Barnes, 2007),

$$\dot{H}_\mathrm{br} = -\frac{1}{2\pi}\sum_a \sum_{b\neq a} \Phi_a \Phi_b \frac{\mathrm{d}\theta_{ab}}{\mathrm{d}t}, \tag{4}$$

where θ_{ab} is the polar angle of the separation vector $\bar{\mathbf{x}}_a - \bar{\mathbf{x}}_b$. This expresses the helicity added to the coronal field as its footpoints are moved about one another. Integrating each of

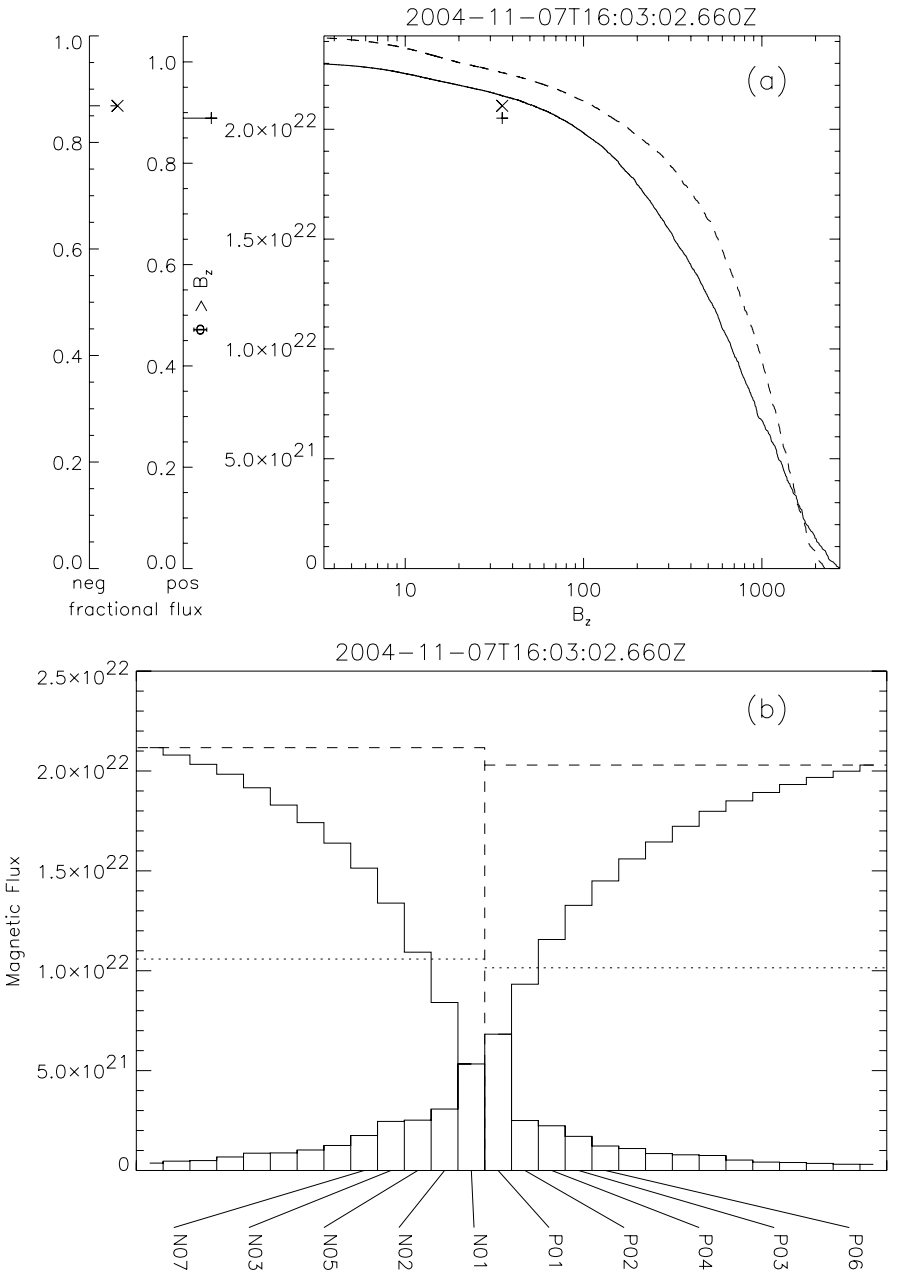

Figure 3 Summaries of the partition at 16:03 UT on 7 November (Figure 2b). (a) Cumulative histograms of the radial field in each polarity. The solid (dashed) curve shows the net positive (negative) flux exceeding a given radial field strength, B_z (the x axis). The $+$ ($\times$) symbols show the amount assigned to partitions, required to have $B_z > 35$ G and $\Phi_a > 7.6 \times 10^{19}$ Mx. (b) A histogram of the different regions at 7 November 16:03 UT. The bars are the different regions ordered by flux labels working from the center; labels are listed under the largest five of each polarity. The accumulations of these are shown as a stair-step curve working outward from the largest region of each polarity. Horizontal dotted and dashed lines mark 50 and 100% of the flux of each sign, respectively.

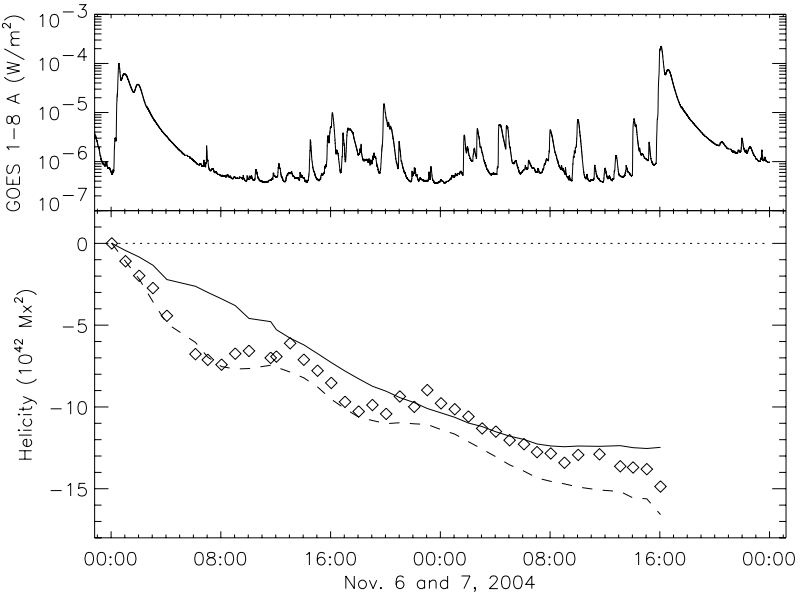

Figure 4 The integrated helicity injected by the photospheric motions (bottom) and the GOES 1 – 8 Å light curve (top). In the bottom panel, the solid curve is the result of applying Equation (3) to the LCT velocity field. The diamonds are the braiding helicity, Equation (4) from the motion of the region centroids and the dashed line is the same for the reduced model.

these expressions from 6 November 00:03 UT shows a steady flux of negative (left-handed) helicity until approximately 7 November 9:00 UT (see Figure 4). Moreover, the braiding helicity of the partitions (diamonds) and of the reduced model (dashed curve) is relatively similar to the actual helicity flux (solid line). This gives some confidence that the centroid motions of our source regions capture the likely driver for the flare: helicity injection.

We proceed under the assumption that AR 10696 had been somewhat relaxed by the large M flares in the first hour of 6 November, and then became increasingly stressed by subsequent photospheric motions. The success of the reduced model, which excludes any flux emergence or submergence, suggests that braiding alone accounts for most of the helicity injection, and perhaps for the pre-flare stressing. From inspection of Equation (4) it can be seen that negative helicity is injected by opposing regions (*i.e.*, $\Phi_a \Phi_b < 0$) rotating about each other in a clockwise sense. In the present case the clockwise motion appears as a shearing along the PIL. It remains to quantify how much energy this shearing stores in the coronal field and how much flux is reconnected to release this energy.

2.2. The Coronal Field Model

To estimate the energy storage we construct a model of the coronal field. The primary use of this model will be to quantify the coronal flux interconnecting photospheric flux regions. We refer to the set of coronal field lines interconnecting a pair of opposite sources, a and b, as a domain, and we denote its net flux $\psi_{a/b}$.

To calculate the domain fluxes we must extrapolate the field from magnetograms. A potential extrapolation from a single unipolar region can be formally expanded as a series of multi-polar terms beginning with the monopole (Jackson, 1975). The first two terms of

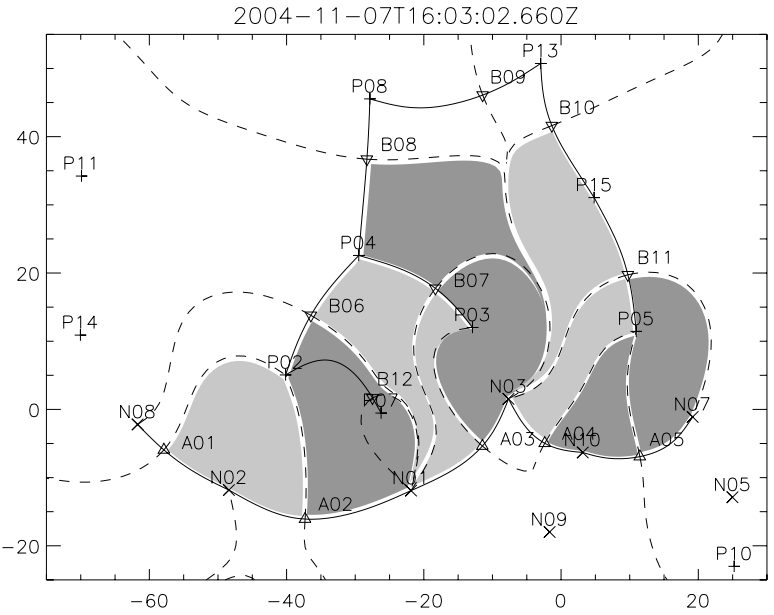

Figure 5 Elements of the skeleton footprint characterizing the topology of the model field at 7 November 16:03, plotted on the tangent plane; axes are in Mm from the point of tangency. Positive and negative sources are indicated by + and × symbols, respectively, positive and negative null points (all photospheric) by ▽ and △ symbols, respectively. Solid lines are the spine curves and dashed lines are the photospheric footprints of fan surfaces (separatrices). Reconnected domains are shaded according to whether they gained (dark) or lost (light) flux.

this series are matched if the region is replaced by a point charge of strength $q_a = \Phi_a/2\pi$, located at the centroid $\bar{\mathbf{x}}_a$. Following this procedure we model the field from all regions is by placing a set of point charges on the photospheric surface; this expedites the assessment of the field's connectivity. The centroid locations are projected from the image plane onto a plane tangent to the solar surface. The plane's coordinate origin is its point of tangency, which rotates with the differential solar rate (Howard, Gilman, and Gilman, 1984), so any motion within the plane represents proper motion on the solar surface. Although this point-charge model has numerous artifacts it yields a reasonably good approximation to the domain fluxes in a continuous potential field: our sole objective.

Both the actual non-potential field and the simplified point-charge field consist of domains separated by separatrix surfaces (Longcope, 2001). In the case of the potential point-charge field all separatrices are the fan surfaces of magnetic null points. A complete map of the field's connectivity can therefore be readily obtained beginning with the null points (Longcope and Klapper, 2002). Figure 5 summarizes the footprint of the field at 7 November 16:03 UT, showing several of the flux domains that will turn out to be significant.

We calculate the domain fluxes $\psi^{(\mathrm{v})}_{a/b}$ in the evolving potential field using a Monte Carlo method described in Barnes, Longcope, and Leka (2005), whereby field lines are initiated from each point charge in random directions and followed to their opposite end. In our case, each field line represents $\psi_0 = 6.67 \times 10^{17}$ Mx of flux, so any domain with $\psi_{a/b} \geq 10^{18}$ Mx will be found with 95% probability (Barnes, Longcope, and Leka, 2005), and the fluxes of larger domains will be determined with statistical uncertainty scaling with $\sim\sqrt{\psi_{a/b}/\psi_0}$.

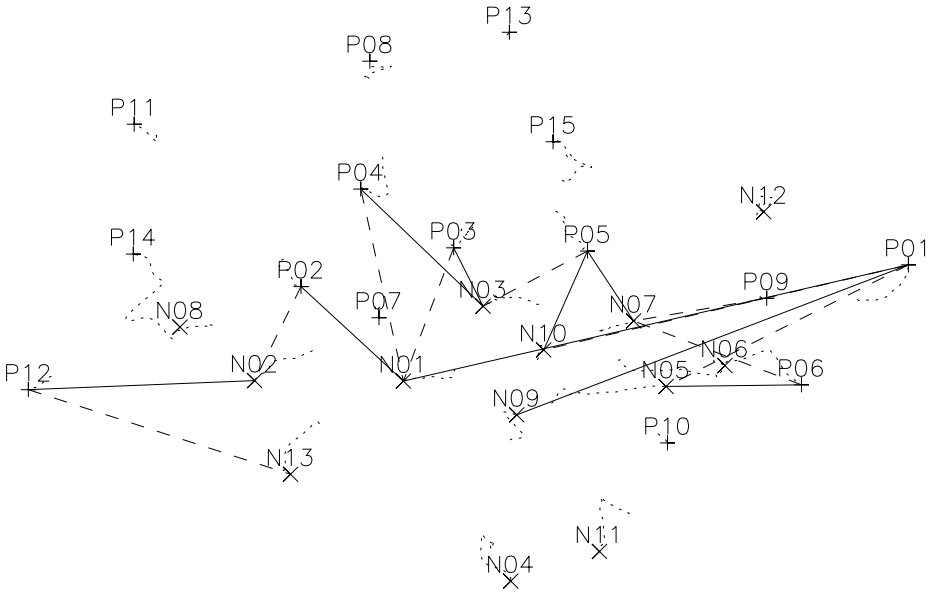

Figure 6 A summary of the evolution of the potential field in response to photospheric evolution. Point charges at 7 November 16:03 UT are indicated by + and × symbols, as in Figure 5. A dotted curve shows the path taken by the charge on the co-rotating tangent plane. Solid (dashed) lines connect each pair whose potential-field domain flux has increased (decreased) by more than 0.3×10^{21} Mx between 6 November 00:03 UT and 7 November 16:03 UT.

Values from the beginning (6 November 00:03 UT) and end (7 November 16:03 UT) of the sequence are listed in Table 1.

The domain fluxes of the potential field change owing to the charge motions, which are also responsible for injecting helicity. A graphical synopsis of the major flux changes, Figure 6, shows the signature of the clockwise shear. Eastward motion of the negative regions, N02, N01, and N03, leads to decreases in their Westerly connections and increases in their Easterly connections. This is the manifestation of the helicity injection in our model coronal field.

Under the assumption that no reconnection occurs between the flares (the first hour of 6 November and the X2 flare at 7 November 15:42 UT), the domain fluxes could not have changed and the field could not have remained in the potential state. In this way the lack of reconnection leads to a storage of free magnetic energy, energy above that of the potential field, which could then be released by reconnection. To achieve the maximum energy release the field would need to relax to its potential state. In other words reconnection will need to transfer flux out of domains for which $\Delta\psi_{a/b}^{(v)} < 0$ and into domains for which $\Delta\psi_{a/b}^{(v)} > 0$. It is this flux transfer by reconnection that was responsible for the X2 flare beginning at 7 November 15:42 UT.

3. The Flare

The X2 flare was observed by TRACE (Handy *et al.*, 1999) at 1 600 Å with 2 – 4 s cadence from 15:36 to 16:40 UT (Figure 7). The two flare-ribbons become visible in the 1 600 Å images at 15:42 UT, at which point they are very close together. The TRACE field of view

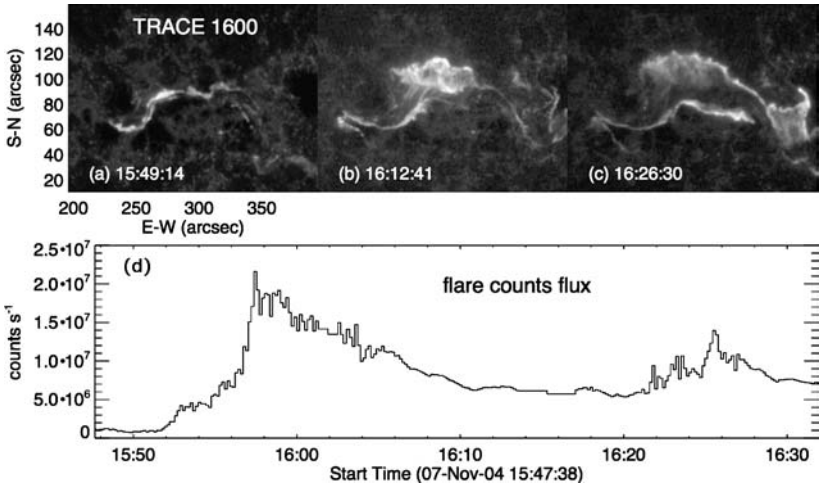

Figure 7 (a) – (c) Snapshots of flare ribbons observed at 1 600 Å by TRACE. (d) Time profile of counts rate integrated in flare region.

(FOV) is 256″ by 256″, which covers nearly the entire flaring region, judged from EIT full-disk observations. We subtract a dark-current value of 87 from these images and then normalize them to a 1-s exposure. They are not, however, normalized by flats as the TRACE flat field will still bring about 15% uncertainties (Qiu *et al.*, 2000; Nightingale, 2000) across the FOV. Instead, we assume that the flare region is reasonably flat and perform no correction. Furthermore, as the flare ribbons are large and much brighter than the background, errors from lack of flattening are not expected to be significant in comparison with other types of errors discussed in the following.

3.1. Measuring Magnetic Reconnection Flux from Flare Ribbons

The 1 600 Å images are mutually coaligned to sub-pixel accuracy by cross-correlating to a common non-flaring reference region. The set is then coaligned with a 5-min-averaged MDI magnetogram centered at 15:11 UT, by using pointing information for the first step and then by registering common features in plage regions. This produces coalignment to better than 2″, the pixel size of MDI magnetograms. To facilitate further analysis we use only a subset of 1 600 Å images with a cadence of around 10 s.

As flare ribbons are formed in the transition region or upper chromosphere, we extrapolate the MDI photospheric magnetogram to 2 000 km upward as a potential field. Shown in Figure 8, the extrapolation smoothes the magnetogram but does not modify the basic magnetic morphologies of the region.

The total reconnected flux is the sum of fluxes in all pixels that brightened, in 1 600 Å, during any period of the flare (see Figure 8). This procedure implicitly assumes that a pixel is not brightened more than once. The assumption is equivalent to one that a single magnetic field reconnects only once in a flare.

Many sources of uncertainty must be accounted for to estimate the uncertainty in the final measurement. We find that it is most important to determine a lower cutoff value in 1 600 Å brightening that defines brightened ribbon areas. This is done largely by trial and error. In this particular event, we adopt a level 16 times the median (count) intensity of a

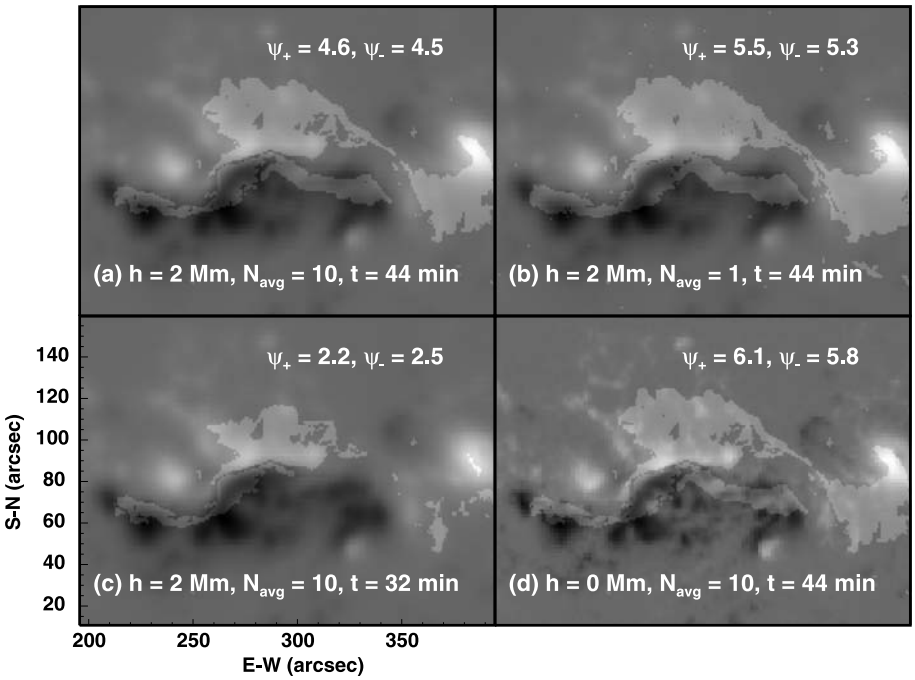

Figure 8 Total area of flare ribbons (shaded), and the encompassed fluxes Ψ_+ and Ψ_-, determined in various ways, superimposed on longitudinal magnetograms (gray scale). The total signed reconnection fluxes are given (in units of 10^{21} Mx) in each situation. In panels (a) – (c), the magnetogram extrapolated to $h = 2$ Mm above the photosphere is used, and panel (d) shows the MDI photospheric ($h = 0$ Mm) magnetogram. Panels (a), (c), and (d) show the flaring area derived by using 10-frame running-mean images, and (b) shows the case using the unsmoothed 10-s-cadence images. In panels (a), (b), and (d), the flare region is measured throughout the duration of the flare ($t = 44$ min), and panel (c) shows the case using images up to 16:20 UT ($t = 33$ min) before the second emission peak (Figure 7). In all panels, the cutoff counts intensity is 16 times the median of the quiescent background counts intensity. The FOV of the images is the same as in Figures 7a – c.

non-flaring reference region as the cutoff. Any pixel that exceeds this value is counted as a flare pixel. Experimentation with cutoff values from a very wide range (9 to 24) resulted in $\pm 25\%$ change in the measured flux; this could be regarded as upper bound in the cutoff contributions to uncertainty.

Potentially significant measurement errors can result from misalignment between images, particularly between the MDI and TRACE data. To quantify its possible contribution we perform a set of trials whereby magnetogram and 1 600 Å images are offset by up to $4''$ (2 MDI pixels). The extreme case is found to bring about 20% change in the measured flux. The standard deviation of a set of misaligned measurements is adopted as the uncertainty, which is 5 – 10% of the measured mean reconnection flux.

Some transient non-ribbon features, such as brightened coronal loops or cosmic rays, will inevitably be included among ribbon pixels. We have found that a typical ribbon pixel remains bright for at least several minutes, whereas transient features do not. We therefore suppress transient features without affecting ribbon pixels by analyzing a running average of $N_{\rm avg} = 10$ frames (*i.e.*, 100 s). Figure 8 shows that cosmic-ray pixels and post-flare loop pixels present in an unaveraged image (Figure 8b) are absent from a 10-frame average (Figure 8a). We have found this approach to also improve significantly the balance between

positive and negative fluxes (a physically sensible balance) in other events not reported in the present paper.

We obtain, from the analysis just described, the total reconnected fluxes as the mean values from measurements at various alignments and ribbon-edge cutoff values. Uncertainties are estimated from the standard deviations in a set of measurement varied in the manners outlined here. The total positive and negative reconnection fluxes are

$$\Psi_+ = 4.8 \pm 0.3 \times 10^{21}\ \mathrm{Mx}, \qquad \Psi_- = 4.6 \pm 0.6 \times 10^{21}\ \mathrm{Mx}, \tag{5}$$

respectively. These values increase if unaveraged 1 600 Å images are used (*i.e.*, $N_{\mathrm{avg}} = 1$) since these count transient features along with the actual ribbons (Figure 8b). Using extrapolated magnetograms results in a 25% decrease in the measured flux when compared to raw photospheric magnetograms (Figure 8d). All cases do, however, maintain a good balance between the positive and negative fluxes.

The present situation is somewhat complicated by the two-phase morphology of this particular flare. The time profile of the total TRACE counts in the flare regions (Figure 7d) indicates two emission peaks roughly 15 minutes apart. These two phases come from different parts of the active region. The second phase (after 16:20 UT) comes mostly from the Western portion (Figure 7c), including the large positive region, P01. This flux region is not involved in the first phase.

The flux reconnected in the first phase, excluding the Western portion, can be calculated by using only the pixels that have brightened by 16:20 UT (*i.e.*, 32 minutes from the beginning of our analysis at 15:48 UT). This integration yields reconnected flux estimates of

$$\Psi_+ = 2.3 \pm 0.2 \times 10^{21}\ \mathrm{Mx}, \qquad \Psi_- = 2.6 \pm 0.5 \times 10^{21}\ \mathrm{Mx}. \tag{6}$$

Ribbon motion persists within the main (Eastern) region even after 16:20 UT, so these values will be an underestimate of the flux reconnected within that section of the AR.

3.2. The Reconnecting Domains

Superposing the spines from the model field onto the 16:20 UT TRACE 1 600 Å image, after advancing the tangent plane 17 minutes, gives an indication of which domains were reconnected during the first phase of the flare. This superposition, shown in Figure 9, when compared to the bare skeleton map Figure 5, suggests that the Southern ribbon follows the spines connecting nulls A01 – A05, and the Northern ribbon the spines connecting B06, B08, B10, and B11. These spines presumably form the footprint of a combination of separatrices that overlay domains affected by the reconnection. The footprints of affected domains are shaded in Figure 5.

The conclusion of this analysis is that the first phase of the two-ribbon flare was the result of reconnection transferring flux out of domains such as P02 – N02, which have more flux than a potential field requires, and into the domains such as P02 – N01, which have less. The domains in Figure 5 are shaded light (dark) if they have an excess (deficit) of flux compared to the potential field. This transfer permits the field to become more potential and therefore releases stored energy.

The complete set of intra-ribbon domains are those connecting the sources on or inside the ribbon-spine sequence in Figure 9. The positive sources are, from East to West, P02, P04, P07, P03, P15, and P05; the negative sources are N02, N01, N03, N10, and N07. All of the sources are included in Table 1, which also includes P01 as its top row. The footprints of the domains connecting the same sources are shaded in Figure 5. The pre-reconnection

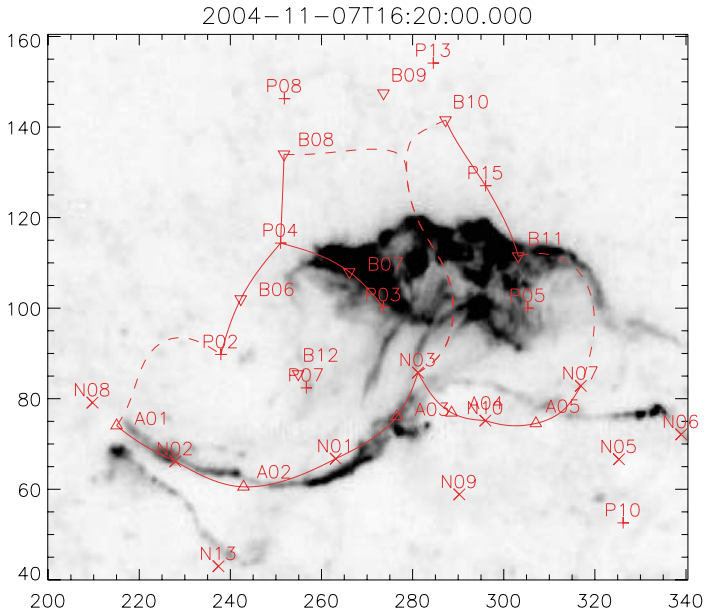

Figure 9 TRACE 1 600 Å image, plotted as reverse gray scale, with elements of the skeleton superimposed. The skeleton is the same one from Figure 5 but projected onto the sky after its tangent plane has been rotated to the time of the TRACE observation (7 November 16:20 UT). Axes are in arcseconds.

Table 1 A table of domain fluxes $\psi^{(\mathrm{v})}_{a/b}$ and their changes $\Delta\psi^{(\mathrm{v})}_{a/b}$ from selected source regions; all values are in units of 10^{21} Mx. Each row or column is one of the largest positive or negative sources. Each entry gives the fluxes at 6 November 00:03 UT (upper left) and 7 November 16:03 (lower right) and the net change (center); a dash indicates that no connection exists between those sources. The far right column and bottom row give the total source flux of that region. These are greater than the sums across the rows or columns owing to the contributions of omitted sources.

	N01	N02	N03	N07	N10	Φ_a
P01	$^{0.73}+0.64_{1.37}$	$^{0.00}+0.05_{0.05}$	$^{0.09}-0.09_{0.00}$	$^{0.72}+0.09_{0.81}$	$^{0.68}-0.34_{0.34}$	6.82
P02	$^{0.03}+1.01_{1.04}$	$^{2.15}-0.77_{1.38}$	–	–	–	2.50
P03	$^{0.95}-0.84_{0.12}$	–	$^{0.67}+0.90_{1.57}$	–	$^{0.04}-0.04_{0.00}$	1.71
P04	$^{1.85}-0.36_{1.49}$	$^{0.21}+0.18_{0.40}$	$^{0.03}+0.27_{0.30}$	–	$^{0.12}-0.12_{0.00}$	2.24
P05	–	–	$^{1.08}-0.88_{0.20}$	$^{0.02}+0.58_{0.61}$	$^{0.00}+0.30_{0.30}$	1.10
P15	$^{0.00}+0.00_{0.00}$	$^{0.00}+0.00_{0.00}$	$^{0.60}-0.24_{0.36}$	$^{0.18}+0.00_{0.18}$	$^{0.02}+0.23_{0.25}$	0.78
Φ_b	5.33	3.08	2.46	1.75	0.88	

domain flux is whatever it was at the beginning of the stressing: $\psi_{a/b} = \psi^{(\mathrm{v})}_{a/b}(0)$, if the field began in its potential state at 6 November 00:03 UT. This differs from the potential field value by

$$\Delta\psi_{a/b} = \psi_{a/b} - \psi^{(\mathrm{v})}_{a/b}(t) = -\Delta\psi^{(\mathrm{v})}_{a/b}.$$

This means that domains with excess flux (relative to the potential field) are those with $\Delta\psi_{a/b} > 0$; these are *negative* values in Table 1 (P02 – N02 for example). The total flux

excess of all intra-ribbon domains, $\Delta\Psi_{\downarrow}$, can be found by summing all the negative entries in the table excluding the top row; the total flux deficit is similarly found by summing the positive entries. These give two estimates for the net flux transfer that must occur in the first phase of the two-ribbon flare:

$$\Delta\Psi_{\downarrow} = 3.25 \times 10^{21}\ \mathrm{Mx}, \qquad \Delta\Psi_{\uparrow} = 3.47 \times 10^{21}\ \mathrm{Mx}. \tag{7}$$

The arrows indicate the sense the fluxes will change under reconnection: Those with an excess will decrease, whereas those with a deficit will increase. Were it not for connections outside the inter-ribbon set these two quantities would exactly match, since one domain's increase comes from another domain's decrease.

These two estimates, which roughly agree with one another, are based on the assumption that every region within the ribbons underwent all the reconnection necessary to return it to a potential state. The analysis defines as reconnection only those changes to a field line's topology that change footpoints from one photospheric source region to another. This is only a fraction of the total flux in all of the source regions on the ribbon. Summing Φ_a for these, listed in the final row and column of Table 1, gives 8.33×10^{21} Mx (positive excluding P01) and 13.49×10^{21} Mx (negative). It seems that only half to one-third of the field anchored to these source regions has been stressed to the point that reconnection is warranted (*i.e.*, would be energetically favorable).

The second phase of the flare involves reconnection to the large positive source P01 as well as P06 and P09 located to the West. In addition to the connection listed in Table 1 there are negative sources, N05 and N06, participating in this second reconnection phase (see Figure 6). Including these domains in our sum yields an estimate for reconnection over both phases of

$$\Delta\Psi_{\downarrow} = 5.52 \times 10^{21}\ \mathrm{Mx}, \qquad \Delta\Psi_{\uparrow} = 5.32 \times 10^{21}\ \mathrm{Mx}. \tag{8}$$

These larger numbers are slightly greater than the amount of ribbon-swept flux for the entire flare given in the previous section. It is the amount of reconnection required to return the entire active region to its potential state.

3.3. Estimating the Energy Storage

To understand the details of the reconnection, and estimate the energy it could release, we must use a non-potential model of the coronal field. We use, for this purpose, the MCC model (Longcope, 1996, 2001), in which it is assumed that the field evolves through the sequence of flux-constrained equilibria (FCE) defined as the states of minimum magnetic energy subject to constraints on all its domain fluxes. Each FCE field includes current only on the intersections between its separatrices, called *separators*. These are the only locations at which current is *required* by the constraints, so they are the only sites where it flows in the minimum energy state. The actual field, which need not be in a state of minimum magnetic energy or even in equilibrium, might have currents distributed elsewhere.

The separator currents in the FCE can be estimated from the difference between the flux through the separator in the potential field, $\psi_i^{(\mathrm{v})}$, and the flux it presently has, ψ_i. The latter value is taken to be the value from the potential field at 6 November 00:03 UT, $\psi_i = \psi_i^{(\mathrm{v})}(0)$, so the net discrepancy becomes

$$\Delta\psi_i = \psi_i - \psi_i^{(\mathrm{v})} = \psi_i^{(\mathrm{v})}(0) - \psi_i^{(\mathrm{v})}(t) = -\Delta\psi_i^{(\mathrm{v})}, \tag{9}$$

where $\Delta\psi_i^{(\mathrm{v})}$ is the change over time in the potential value.

Table 2 Properties of the eight separators of the ribbon separatrices, listed by their index by i shown in Figure 10. Listed are topological properties, the names of the nulls linked by the separator, and the principal domain enclosed by it and geometrical properties, the length L, and maximum altitude $z_{\max}$, of the separator in the potential field at 7 November 16:03 UT. The flux discrepancy, $\Delta\psi_i$, between that field and the initial one (6 November 00:03) leads to the current I_i, which in turn leads to self-free-energy ΔW_i and helicity H_i on each separator.

i	Nulls		Encloses	L	$z_{\max}$	$\Delta\psi_i$	I_i	ΔW_i	H_i
	−	+		(Mm)	(Mm)	(10^{21} Mx)	(GA)	(10^{30} ergs)	(10^{42} Mx^2)
1	A01	B06	P02 – N08	43.9	8.7	−0.23	−24.2	0.06	−0.05
2	A02	B06	P02 – N01	55.0	18.6	−1.01	−465.4	17.79	−2.92
3	A02	B08	P04 – N02*	127.3	42.6	−0.79	2.7	0.00	0.04
4	A03	B08	P04 – N03*	91.2	28.7	−1.11	−65.4	0.73	−0.72
5	A03	B07	P03 – N01	35.3	10.8	−0.84	−562.6	14.98	−2.29
6	A04	B10	P15 – N03*	97.2	32.3	−1.13	−97.7	1.45	−1.17
7	A04	B11	P05 – N03	36.1	9.8	−0.88	−948.4	29.06	−3.16
8	A05	B11	P05 – N10*	39.0	11.7	−0.59	57.3	0.31	0.19
Total						−6.57		64.38	−10.09

*The largest of several domains included by the separator.

The current on each separator of the FCE is estimated by using the discrepancy $\Delta\psi_i$ and properties of the separator field line in the potential field (Longcope and Silva, 1998; Longcope and Magara, 2004). Although in making this estimate it is assumed that the current causes only local distortions to the potential field, at least one analytically tractable example shows reasonably good agreement well outside this regime (Longcope and Magara, 2004). When computed in isolation from the other separators the function $I_i(\Delta\psi_i)$ is monotonic, yielding a positive current when $\Delta\psi_i > 0$. This means that when a separator encloses more flux than it would in a potential field, its current flows parallel to the magnetic field and thereby contributes positive helicity. Furthermore, reconnection across the separator will transfer flux, reducing $\Delta\psi_i$ and therefore the current.

The potential field at 7 November 16:03 UT has 29 null points, which are linked by at least 32 different separators. Of these only 8 separators connect null points found on the ribbon, which would be embedded in the separatrices involved in the flare's first phase; we therefore focus on these alone (see Figure 10). Table 2 lists these separators along with the nulls they interconnect, their length, and maximum height. The separator currents are calculated by including interaction between each other, akin to mutual inductances (Longcope and Magara, 2004). The direct energetic contribution of each separator is listed in the column second from the right. The sum of these entries is listed at the bottom ($\Delta W = 6.4 \times 10^{31}$ ergs); however, mutual inductances raise the total free energy to $\Delta W = 8.2 \times 10^{31}$ ergs. For comparison, a potential field extrapolated from the MDI magnetogram has an energy $W_{\rm pot} = 145 \times 10^{31}$ ergs, almost constant over the 40-hour interval. Thus the lack of reconnection raises the energy of the magnetic field by less than 6%. It is this energy that may, however, be released simply by local changes in the topologies of a few field lines (*i.e.*, by magnetic reconnection).

Every separator in Table 2 has a negative discrepancy $\Delta\psi_i$ between the present flux (fixed at 6 November 00:03 UT) and the present potential value. This means that the 40 hours of shearing has left all the separators enclosing less flux than they would in a potential field. In

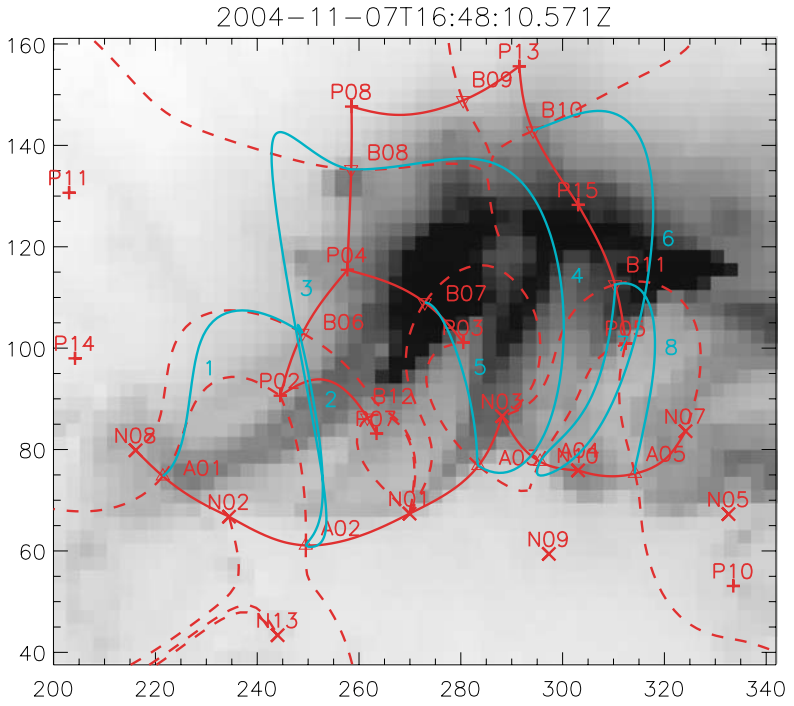

Figure 10 195 Å image from SOHO/EIT (inverse gray scale), superposed with the footprint from Figure 5 (red) and separators (blue).

the absence of interactions this negative discrepancy would drive negative current; however, Table 2 shows that in two cases (separators 3 and 8) the contributions of other currents actually reverse it. This current will flow along the separators of the field that will naturally become distorted. This collection of deformed currents are the three-dimensional analog of the current that forms in two-and-a-half dimensional sheared arcade models (Mikic, Barnes, and Schnack, 1988).

Since it is not the potential field, the FCE field can have a non-vanishing relative helicity. This can be approximated as a sum over the currents in the separator current sheets (Longcope and Magara, 2004). Table 2 lists each of the terms, which naturally have the same sign as the current, and the net helicity of all contributions at the bottom. This value, $H \simeq -10^{43}$ Mx^2, accounts for most of the helicity injected by the motions of the model flux sources, shown in Figure 4. The latter value will contribute to current flowing in the other 24 separators so it is somewhat larger. We are explicitly considering the ones nearest the PIL, which probably contain a larger share of helicity. Even among the eight separators we consider, the shortest two (5 and 7) account for a disproportionate share of the free energy and relative helicity.

The model's energy release can be compared to observation by estimating the GOES light curves it would produce. Warren and Antiochos (2004) performed a series of gas dynamic simulations in static loops of circular cross section subject to energy deposition by non-thermal electrons. They arrived at empirical expressions for peak fluxes in each of the GOES channels (1 – 8 Å and 0.5 – 4 Å) in terms of the volume V, length L, and total energy

Table 3 Summary of the recipient domains from the three most energetic separators. Recipient domains for separators σ_i, where $i = 2, 5, 7$, are listed along with their dimensions in a potential field: $\psi_{a/b}^{(v)}$, $V_{a/b}$, and $\langle L \rangle$. The values of energy E_f and volume V_f are used in a flare model to yield the peak GOES fluxes listed in the right columns.

i	Recipient domain	ψ_i (10^{21} Mx)	$\psi_{a/b}^{(v)}$ (10^{21} Mx)	$\langle L \rangle$ (Mm)	$V_{a/b}$ (10^{27} cm^3)	V_f (10^{27} cm^3)	E_d (10^{30} erg)	E_f (10^{30} erg)	F_{1-8} (10^{-6} W/m^2)	$F_{0.5-4}$ (10^{-6} W/m^2)
2	P02 – N01	1.01	1.05	33.8	4.27	4.12	4.45	4.45	127.9	22.0
2	P04 – N02	1.01	0.37	87.9	30.29	30.29	4.45	1.61	3.8	0.2
5	P04 – N01	0.84	1.53	64.2	46.27	25.34	3.74	3.74	20.6	1.8
5	P03 – N03	0.84	1.58	20.9	3.18	1.69	3.74	3.74	208.3	40.3
7	P05 – N10	0.88	0.31	25.9	1.26	1.26	7.26	2.53	123.7	25.3
7	P15 – N03	0.88	0.33	53.4	8.45	8.45	7.26	2.76	29.0	3.5
	Total				93.72	71.14	30.92	18.84	513.4	93.2

deposition E. When these are expressed in cgs units the peak fluxes, in W/m^2, are

$$F_{1-8} = 3.7 \times 10^{-35} \left(\frac{EL}{V} \right)^{1.75} \frac{V}{L^2},$$
$$F_{0.5-4} = 4.4 \times 10^{-42} \left(\frac{EL}{V} \right)^{2.24} \frac{V}{L^2}. \quad (10)$$

In spite of our more complicated magnetic geometry we apply the empirical relationships, Equation (10), to our flare. We consider only separators 2, 5, and 7, since their self-energies W_i account for a majority of the total stored. We begin by calculating the volume $V_{a/b}$ and average field line length $\langle L \rangle$ for each of the recipient domains in the potential field (see Table 3). We assume that the separator energy W_i is converted into energetic electrons with an efficiency of 50% and that an equal share, $E_d = 0.25 W_i$, is deposited into each side of the post-reconnection flux. If the potential flux in a recipient domain is greater than the transferred flux, $\psi_{a/b}^{(v)} > \Delta\psi_i$, then we assume that the flare occupies a fraction of the domain's volume, $V_f = (\Delta\psi_i / \psi_{a/b}^{(v)}) V_{a/b}$, with all of the energy deposited in that flux ($E_f = E_d$). Otherwise we assume that the flare occupies the full domain volume, $V_f = V_{a/b}$, but with only a fraction of the energy $E_f = (\psi_{a/b}^{(v)} / \Delta\psi_i) E_d$, the remainder presumably following the reconnected flux in subsequent reconnections, described further in the following section. The application of these assumptions to the six recipient domains of the three separators is summarized in Table 3.

The single brightest flaring domain, P03 – N03, has an estimated peak flux $F_{1-8} = 2.1 \times 10^{-4}$ W/m^2, in agreement with the actual GOES observation (2.2×10^{-4} W/m^2). The observed peak in the 0.5 – 4 Å channel, 6.2×10^{-5} W/m^2, is slightly higher than the modeled value, 4.0×10^{-5} W/m^2, suggesting that some aspect of our simple model is not accurate. Each of the other separators has one domain whose flux is about 60% as high as that of P03 – N03 (namely P02 – N01 and P05 – N10). This fact could lead to the type of broad or multi-peaked GOES light curve actually observed in this case (see top panel of Figure 4), as the reconnection occurred at slightly different times on the different separators. Were all the reconnection to occur at once the fluxes would add up to $F_{1-8} = 5.1 \times 10^{-4}$ W/m^2 (bottom row of Table 3), which is greater than observed. The main point of this exercise is to confirm that the energy storage predicted by the model is not inconsistent with the observed X-ray flare.

4. Flux Rope Creation

4.1. Separator Reconnection

Flux transfer between domains can occur only across a magnetic separator (Sweet, 1958; Longcope, 2001). Since it forms the intersection between two separatrices, a separator abuts four different flux domains simultaneously. It is in this sense that the separator is analogous to an X-type neutral point in two-dimensional reconnection. Flux from two donor domains is destroyed by conversion into flux for two recipient domains. The non-ideal process by which the conversion occurs is not as important to the present discussion as the requirement of some electric field parallel to the separator. The separator consists of magnetic field lines, so the reconnection electric field must have a non-ideal origin: It cannot be related to $\mathbf{v} \times \mathbf{B}$.

Every separator has two donor domains, whose flux is decreased, and two recipient domains, whose flux is increased by the same amount. The distinction between donor and recipient is made by the sign of the net flux discrepancy of the domains it encloses. Many domains are adjacent to multiple separators and can therefore serve as both donors and recipients. Figure 11 provides a schematic depiction of this interrelation for the model field at 7 November 16:03 UT. Domains are represented by circles containing the indices of their positive and negative sources in the format P/N; in several cases two domains share a circle in the interest of clarity. The circles are arranged so that diagonals have a common positive or negative source (for illustration, the diagonals for N03 and P04 are indicated by arrows). Each separator is designated by a pair of crossed lines with arrows pointing to the recipient domains. The lowest portion of the diagram therefore shows that separator 1 converts flux from donor domains P04 – N02 and P02 – N08 to flux in recipient domains P02 – N02 and P04 – N08. The reconnection process must break in half field lines from each donor domain and rejoin them into field lines of the recipient domains, with their footpoints interchanged.

It turns out that reconnection must often occur in a particular sequence. Shaded circles are domains with a deficit of flux relative to the potential field, $\Delta\psi_{a/b} < 0$, which can be eliminated by receiving flux via reconnection. In some cases, however, the donor domains themselves are flux-deficient. Domain P04 – N02, for example (labeled $4/2$ and found in the center of the third row from the bottom), has a discrepancy $\Delta\psi_{4/2} = -0.19 \times 10^{21}$ Mx and is a donor domain for both separators 1 and 3. We expect that reconnection across these two separators will not, therefore, begin until reconnection has first occurred across another separator for which this domain is a recipient, separator 2 for example. Thus in this example there must be reconnection first on separator 2 and later on separators 1 and 3.

It is possible, by using Figure 11, to deduce all such dependencies. To simplify the analysis we focus on those domains from the set we believe are connected to the flare ribbons; these are designated by solid circles. We assume that the other domains (external domains with dotted circles) will undergo reconnection through more distant separators to eliminate any flux deficits. Whenever a separator contains a donor with a deficit, its reconnection is contingent on a separator from which that particular domain is a *recipient*. In this way we may deduce a set of contingencies, denoted by dotted arrows. Certain pairs, such as separators 4 and 11, are contingent upon one another so a third reconnection is required to break the stalemate. The flare must begin with reconnection at a separator from which all arrows point outward. Only separators 2 (near the bottom) and 7 (near the top) have this property, so it is from these outer separators that the two-ribbon flare must have begun. Separator 4, in contrast, can only undergo reconnection after the following sequence of separators have first reconnected: 7 – 6 – 11.

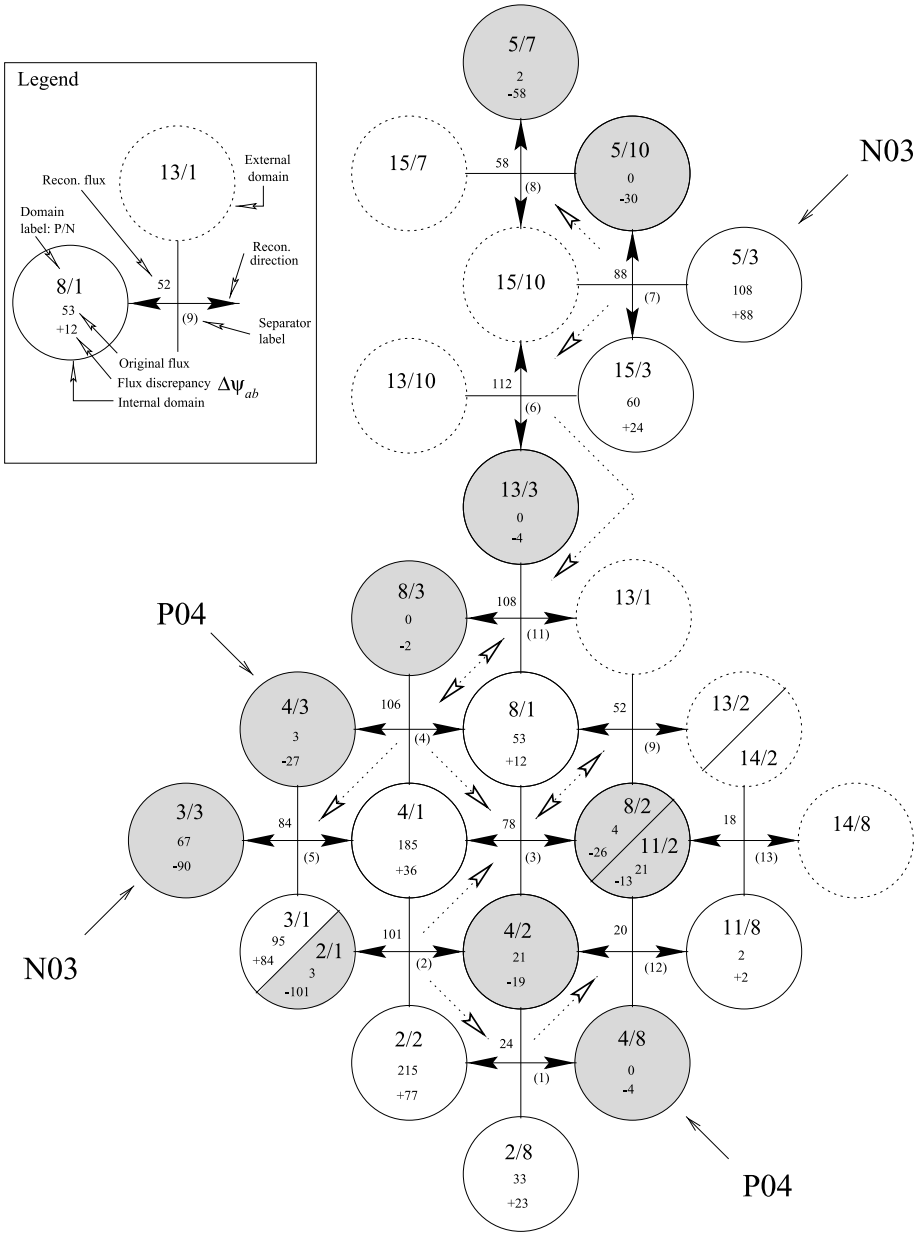

Figure 11 Schematic depiction of reconnection sequences. Domains are represented by circles containing a label P/N. They also include the values of their pre-flare domain flux, $\psi_{a/b}$, and flux discrepancy, $\Delta\psi_{a/b}$, in units of 10^{19} Mx. All domains for which $\Delta\psi_{a/b} < 0$ are shaded. Intersections of vertical and horizontal lines are separators whose reconnection increases or decreases the fluxes in the domains; arrows indicate the sense in which the flux transfer will occur. Dotted arrows indicate that contingency requires reconnection to occur sequentially between two separators.

Multi-step reconnection can play a particularly important role in the creation of a twisted flux rope. When two flux bundles reconnect across a current sheet they create two new bundles of twisted flux. This is the mechanism by which the four reconnection sites in Figure 1b create a single twisted flux rope. The general result is a consequence of helicity conservation, which can be cast as a conversion of mutual helicity of the initial tubes into self-helicity within the final tubes (Wright and Berger, 1989; Chae, 1999). The net relative helicity will change very little since fast reconnection is very localized and the footpoints are virtually stationary over flare time scales (Berger, 1984).

Although the geometry of our model is considerably more complex than previous investigations of mutual-to-self-helicity conversion it is possible to understand the process within the MCC model. The helicity in each of the separator currents (see Table 2) represents mutual helicity between the donor domains (Longcope and Magara, 2004). As reconnection decreases this current, it also decreases the mutual helicity, which must be converted to self-helicity in the recipient domains. The MCC model is not able to represent self-helicity, since it does not constrain the internal structure of a domain. Nevertheless, we expect the flux in the recipient domains to be twisted as a result. If that flux is then passed through a separator in a subsequent reconnection we can expect its helicity to be passed with it, and possibly augmented by the mutual helicity of *that* separator. In this way multi-step reconnection can produce one highly twisted flux tube.

There is a particular sequence of reconnections, beginning at separator 7, that is likely to produce a highly twisted flux tube. Domain 5/3 (upper right of Figure 11) has 0.88×10^{21} Mx of excess flux (88 in units of the figure). Reconnection at separator 7 combines this with external flux from 15/10 to produce fluxes in recipients 5/10 and 15/3. This drives the latter domain up to an excess of 1.12×10^{21} Mx, which it passes through separator 6 into 13/3. Domain 13/3 is an inherently tiny domain so it immediately passes the flux through separator 11 to another tiny domain 8/3, which passes it in turn through separator 4 to a low-lying domain, 4/3, and a long overlying domain, 8/1, shown in Figure 12.

The final transfer of 1.06×10^{21} Mx in the foregoing sequence involves flux that has been passed from domain to domain in four separate reconnections. The intermediate domains retain very little in the process. Simple mutual-to-self-helicity transfer models predict an addition of one-half twist with each reconnection (Wright and Berger, 1989). Applying this to the flux tube linking P08 to N01 would predict that it includes two complete turns, a level above the threshold for kinking. We therefore propose that the flux rope ejected by the two-ribbon flare was the product of this particular reconnection sequence, and therefore it contains

$$\Phi_{\rm ft} \simeq 1.06 \times 10^{21}\ {\rm Mx} \tag{11}$$

of flux. The footpoints of the flux opened by such an eruption would be P08 in the North and N01 in the South. The flux tube would resemble a twisted version of the red lines in Figure 12, at least until the dynamics of eruption produced still other reconnections with still more outlying sources.

There is not yet a quantitative model of helicity transport through a multiple sequence of reconnections in the MCC model. Such a model would need to account for changes in mutual helicity owing to currents that change as a result of mutual inductance. We can, however, use the total amount of mutual helicity contained on separators 4, 6, and 7 in the pre-flare state as an estimate: $\sum H = -5.05 \times 10^{42}\ {\rm Mx}^2$. If half of that mutual helicity ended up as self-helicity in the flux rope, then the ejecta would carry

$$H_{\rm ft} \simeq -2.7 \times 10^{42}\ {\rm Mx}^2. \tag{12}$$

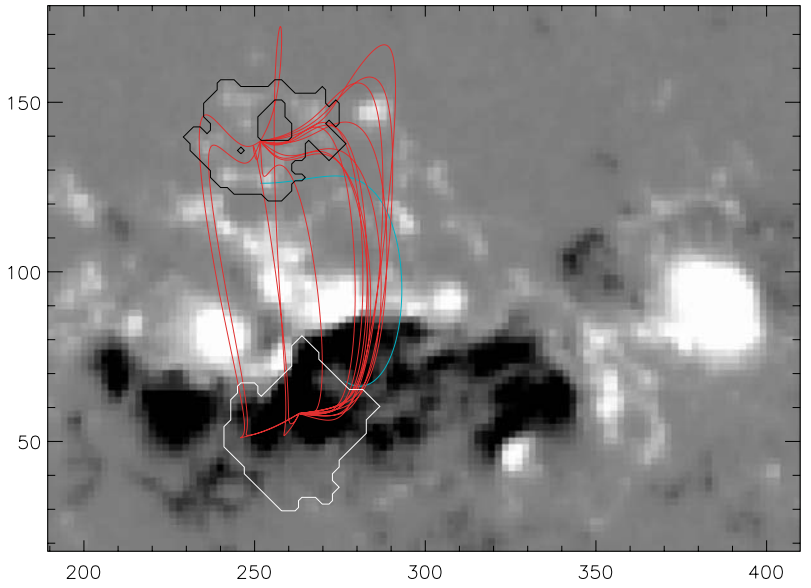

Figure 12 Configuration of domain P08 – N01 (a.k.a. 8/1) in the potential field from 7 November 16:03 UT. Magnetogram is shown in gray scale with regions P08 and N01 outlined in black and white, respectively. The cyan line is separator 4, across which the final reconnection occurs. Red lines are representative field lines from the domain.

A tube of flux $\Phi_{\rm ft}$ with N twists will contain self-helicity $H_{\rm self} = N\Phi_{\rm ft}^2$ (Berger and Field, 1984), suggesting that the ejected tube would have 2.5 left-handed turns, not too different from the half-turn-per-reconnection estimate.

Summing the positive flux discrepancies in all of the internal donor domains in the sequence (5/3, 15/3, 8/1, and 4/1) we predict at least 1.60×10^{21} Mx of ribbon motion associated with producing this flux tube. This illustrates how the creation of twist, through multiple reconnections, explains a discrepancy between the flux reconnected and that in the tube produced.

4.2. The Interplanetary Flux Rope

The interplanetary manifestation of the flare at 7 November 2004 16:15 UT was a magnetic cloud that passed one astronomical unit (AU) about 52 hours later (beginning around 9 November 20:30 UT). *In situ* magnetic measurements of this passage were obtained by the *Wind* spacecraft and have been analyzed by Harra *et al.* (2007). We summarize these observations briefly and describe their relevance to our model of the flare and eruption.

The axially symmetric (cylindrical) magnetic field corresponding to a linear force-free configuration was obtained by Lundquist (1950). It has been shown that this solution is consistent with *in situ* measurements of interplanetary magnetic flux tubes at 1 AU (Burlaga *et al.*, 1981; Burlaga, 1988; Lepping, Burlaga, and Jones, 1990). Thus, the field of MCs is very often relatively well modeled by

$$\mathbf{B} = B_0\big[J_1(\alpha r)\hat{\boldsymbol{\phi}} + J_0(\alpha r)\hat{\mathbf{z}}\big], \tag{13}$$

where J_n is the Bessel function of the first kind of order n, B_0 is the strength of the axial field, and α is a constant associated with the twist at the MC axis. The unit vectors $\hat{\mathbf{z}}$ and

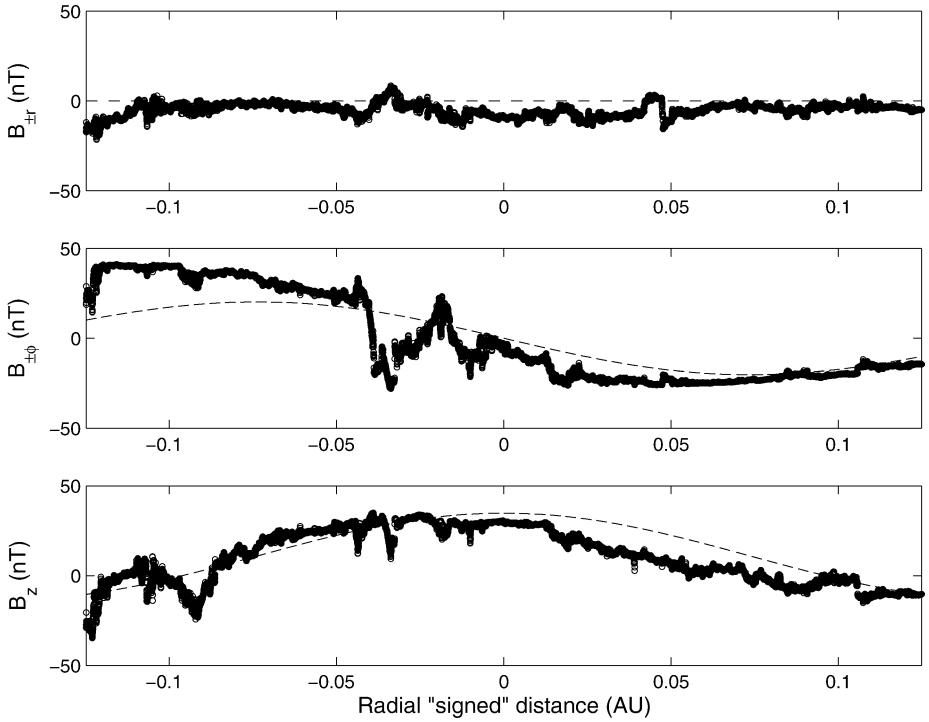

Figure 13 Fitted (dashed curves) and observed (symbols) components of the magnetic field vector inside the magnetic cloud observed by *Wind* from 9 November 2004 at 20:30 UT to 10 November 2004 at 10:00 UT.

$\hat{\boldsymbol{\phi}}$ correspond to the axial and azimuthal directions in a cylindrical system of coordinates, and thus B_r, B_ϕ, and B_z are the components of the magnetic field inside the MC in cloud-centered coordinates.

The axial magnetic flux under the Lundquist's model is given by

$$F_z = 2\pi \int_0^R B_z(r) r \, \mathrm{d}r = 2\pi B_0 R J_1(\alpha R)/\alpha. \tag{14}$$

The azimuthal magnetic flux per unit length (L) along the cloud axis can be computed from

$$\frac{F_\phi}{L} = \int_0^R B_\phi(r) \, \mathrm{d}r = B_0\big[1 - J_0(\alpha R)\big]/\alpha. \tag{15}$$

The relative helicity can be obtained, by taking $\mathbf{A} = \mathbf{B}/\alpha$, from (see, *e.g.*, Dasso *et al.*, 2003)

$$H = \frac{4\pi B_0^2 L}{\alpha} \int_0^R J_1^2(\alpha r) r \, \mathrm{d}r. \tag{16}$$

We analyze here the *in situ* measurements of the magnetic field vector components obtained in Geocentric Solar Ecliptic (GSE) coordinates by the Magnetic Field Instrument (MFI) aboard of the spacecraft *Wind* (Lepping *et al.*, 1995). A left-handed helical magnetic cloud, associated with the material ejected from AR 10696, was observed by *Wind* from 9

November at 20:30 UT to 10 November at 10:00 UT. (For an analysis of the timing and association between the cloud and the AR see Harra *et al.*, 2007.)

We apply a minimum variance method to obtain the main axis of the flux rope (see, *e.g.*, Bothmer and Schwenn, 1998 and Dasso *et al.*, 2005a) and then rotate the observed magnetic field components of the cloud to the local components, finding a radius $R = 0.125$ AU. We then fit the physical parameters (B_0 and α) of the static Lundquist's model from the observed B_ϕ and B_z (see Dasso *et al.*, 2007 for an analysis of an expanding model to this cloud), using a least-squares method, obtaining $B_0 = 34.8$ nT and $\alpha = -25.0$ AU^{-1}. The fitted curve together with the data are shown in Figure 13 versus the "signed" distance to the cloud axis (negative before the spacecraft reaches the cloud center, and positive thereafter). The top panel shows the radial field $B_{\pm r}$ (theoretically expected to be zero), the middle panel the azimuthal component ($B_{\pm\phi}$), and the bottom panel the axial component of the field (B_z). The minus sign in $B_{\pm r}$ and $B_{\pm\phi}$ corresponds to $r < 0$, and the plus to $r > 0$, and it is shown in this way to be a clearer comparison with the time series of **B** observed by the spacecraft.

From the fitted values for B_0 and α, and from expressions given above, we obtain an axial flux of $F_z = 7.2 \times 10^{20}$ Mx, an azimuthal flux of $F_\phi = 8.2 \times 10^{21}$ Mx, and a helicity content of $H = -1.1 \times 10^{43}$ Mx^2 (where we have assumed a flux rope length of 2 AU).

5. Discussion

The foregoing has provided a magnetic model of a particular two-ribbon flare including a 40-hour pre-flare buildup of energy. The model is necessarily complex to match the geometry of the observed AR. In spite of its complexity, the model contains all the basic elements of the CSHKP flare scenario. An active region is sheared along its PIL to build up stress. After this pre-flare buildup, magnetic reconnection occurs, eliminating some or all of the stress and creating a twisted flux rope overlying the AR. The modeling effort thereby demonstrates that the simple two-dimensional model of CSHKP applies in detail to actual solar flares.

The combination of a faithful magnetic model and careful measurements permit us, for the first time, to quantify the CSHKP scenario in three dimensions. The overall shearing is quantified best by magnetic helicity injection: $\Delta H = -1.4 \times 10^{43}$ Mx^2 is injected over the 40 hours of observation. Distributing this helicity through the $\Phi_{\rm tot} = 2 \times 10^{22}$ Mx of the AR would give each field line approximately $\Delta H/\Phi^2 \simeq 1/3$ of a turn in the left-handed sense. Although this value is not negligible, it falls significantly short of one to one and a half turns typically needed for current-driven instabilities such as the kink mode (Hood and Priest, 1979). Moreover, two-dimensional arcade models generally exhibit eruptions only after the tangent of the shearing angle has exceeded 5 – 10 (Mikic, Barnes, and Schnack, 1988; Choe and Cheng, 2000); in this case it would be approximately one-third. It is also noteworthy that the actual helicity injection (solid curve in Figure 4) appears to end roughly eight hours *before* the flare.

Photospheric shearing stresses the magnetic field by separating footpoints that initially face each other directly across the PIL. The minimum current corona model provides an estimate of the energetic consequences of such footpoint motions. In the present case its estimate is that at least 8×10^{31} ergs built up over the 40 hours of shearing. This is a modest 6% above the minimum energy (1.4×10^{33} ergs) of the potential field. In view of the modest amount of shearing observed in the photosphere a modest amount of free energy is not altogether surprising. Using two-dimensional models Klimchuk, Sturrock, and Yang (1988) found that shearing an arcade to an average angle of $\tan^{-1}(S)$ will increase its energy by

an additional $0.78\ln(1+0.55S^2)$ of potential energy. For a shear of $S = 1/3$ this two-dimensional relation yields 5% of the potential energy, in good agreement with the MCC model results.

The most significant advantage of our complicated topological field model is the insight it provides into the reconnection process. Rather than producing one disconnected plasmoid, reconnection in three dimensions transfers flux from one kind of connection to another. In the present case it transfers flux from the connections that have been stretched by shearing into connections that are less stretched. This serves to shorten the field lines, overall, thereby decreasing the magnetic energy. Nor does every field line need to be shortened, owing to the modesty of the shear. The modeling of AR 10696 shows that only $\Delta\Psi \simeq 5.4\times10^{21}$ Mx of flux (from Equation (8)) need be transferred to eliminate all of the shear. This accounts for approximately one-quarter of the flux in either polarity of the AR; it is apparently not energetically favorable to significantly change the connectivity of the remaining three-quarters.

It is not easy to measure how many different field lines have been topologically changed by reconnection. The most reliable means of doing so has proven to be the measurement of the total magnetic flux across which the flare ribbons sweep (Forbes and Priest, 1984; Fletcher *et al.*, 2001; Qiu *et al.*, 2002). Our measurements of the ribbon-swept flux calculated from co-aligned TRACE 1 600 Å images and SOHO/MDI magnetograms in both phases of the flare are in good agreement with the reconnected flux inferred from the MCC model. Furthermore, the ribbons are configured similarly to the separatrices across which the flux transfer should occur. Since the MCC model is topological, as opposed to geometrical, any agreement in actual location must be considered fortuitous. The topological agreement does, however, corroborate the reconnection scenario we infer from the model.

Unlike the simpler two-dimensional case, three-dimensional reconnection need not occur along the entire PIL simultaneously. Instead it occurs sequentially at different separators and the sequence is prescribed by the interrelations among the different connectivities. We find one particular connectivity that can only be produced through a sequence of four different flux transfers. Each flux transfer will add self-helicity, in the form of twist, to the field in the final connectivity. One consequence of this sequencing is the production of a highly twisted flux rope containing significantly less flux than a simple census of all reconnection would predict. This much had been foreseen in previous eruption models (Gosling, 1990), but here we have produced a quantitative model of it for a particular flare.

The model of cascading reconnection in AR 10696 differs from traditional arcade scenarios in the orientation of its flux rope. When the PIL is very long and straight, as in the traditional quasi-two-dimensional arcade, cascading reconnection produces a twisted flux rope anchored to the ends of each polarity band. As suggested by the cartoon of Gosling (1990), the axis of this domain will lie almost parallel to the PIL. Several observational studies have found the orientation of a MC axis to lie close to that of the filament or PIL from which the eruption originated (Marubashi, 1997; McAllister *et al.*, 2001). Our reconnection sequence, however, terminates with a domain, P08 – N01, lying roughly *perpendicular* to the PIL. Indeed, this domain is aligned in the direction dictated by the large-scale dipole moment of the Eastern (flaring) portion of the AR: 60° South of West (with the dipole moment of the photospheric flux being directly opposite to this direction). This state of affairs is the natural one when an AR is less elongated (more dipolar) than model arcades. One previous example of such a case was studied by Webb *et al.* (2000), who found that the axis of the MC was aligned in a direction close to the dipole moment of the AR rather than its PIL. It seems that AR 10696 has this same relatively compact nature, at least in its Eastern portion.

The flux rope in our model, a domain populated by a sequence of four reconnections, has $\Phi_{\rm ft} = 10^{21}$ Mx. The fact that this is less than one-third of all the reconnection that produced

it is a natural result of the multi-stage sequence involved in the two-ribbon flare. A second consequence of the multi-step reconnection is a conversion of mutual helicity to self-helicity in each step, resulting in a flux rope containing $H_{\rm ft} = -2.7 \times 10^{42}$ Mx^2. This corresponds to at least two full turns in each field line, far beyond the one-third of a turn injected by photospheric shearing. Such amplification of twist by reconnection is related to that in the prominence models of Pneuman (1983) and van Ballegooijen and Martens (1989).

The *Wind* spacecraft made observations of a magnetic cloud believed to have been launched during the flare. These measurements show a flux rope with flux comparable to that in the model, although slightly lower. The axis of the MC is oriented toward the Southwest, opposite to the Eastward PIL (Harra *et al.*, 2007) but not so different from domain P08 – N01 and the AR's dipole field. Most puzzling, however, is that the observed flux rope contains a magnetic helicity $H = -10^{43}$ Mx^2, at least four times greater than that of the model flux rope. In light of its lower flux, the observed flux appears to be twisted 20 times rather than the two-and-a-half times in the model. This excess twist might have been introduced by additional reconnections not accounted for in the model. It is also possible that the flux rope is not as uniformly twisted as we had assumed and that *Wind* observed the most tightly twisted part of a rope with fewer than 20 turns.

Lacking any evidence for non-uniform twist we can only meaningfully discuss the first hypothesis: The flux rope's helicity is due to reconnection beyond what our model had included. It seems implausible that this extra reconnection occurred within the AR, since the flux rope helicity is roughly as great as the total amount injected into the AR during the 40-hour buildup. Under typical reconnection scenarios only half of the helicity content of the AR could be transferred into the ejected flux rope; the remainder would remain in the shortened domains. The natural alternative would be to postulate that the flux rope underwent subsequent reconnection with field outside the AR. Indeed, observations of the larger corona suggests that the flux rope observed by *Wind* is not anchored entirely within AR 10696, but instead it straddled a filament separating AR 10696 from the Southern hemisphere AR 10695 (Harra *et al.*, 2007). Our present modeling is not up to the task of investigating this possibility quantitatively. At present we can only speculate that subsequent flux transfers between AR domains and interlinking domains would maintain a rope of roughly constant flux. Mutual helicity between these domain that arose from relative AR motions would be converted into self-helicity of the final flux rope.

Acknowledgements This work was initiated at a workshop funded under the Philip Leverhulme award, held at the Mullard Space Sciences Laboratory, UCL, in June 2005. We are grateful to the organizer, Louise Harra, and to MSSL for hospitality. We thank the workshop's other participants, especially Nancy Crooker, for discussions. The work was supported by NASA (C.B. and G.B.), the U.S. Department of Defense (D.L. and B.R.), and the National Science Foundation (J.Q.) and under the Argentinean grants UBACyT X329, PIP 6220 (CONICET), and PICT 03-14163 (ANPCyT). S.D. is a member of the Carrera del Investigador Científico, CONICET. This research made use of NASA's Space Physics Data Facility (SPDF) and of NASA's Astrophysics Data System (ADS) Bibliographic Services.

References

Barnes, G., Longcope, D.W., Leka, K.D.: 2005, *Astrophys. J.* **629**, 561.
Berger, M.A.: 1984, *Geophys. Astrophys. Fluid Dyn.* **30**, 79.
Berger, M.A., Field, G.B.: 1984, *J. Fluid. Mech.* **147**, 133.
Berger, T.E., Lites, B.W.: 2003, *Solar Phys.* **213**, 213.
Bothmer, V., Schwenn, R.: 1998, *Ann. Geophys.* **16**, 1.
Burlaga, L.F.: 1988, *J. Geophys. Res.* **93**, 7217.
Burlaga, L., Sittler, E., Mariani, F., Schwenn, R.: 1981, *J. Geophys. Res.* **86**, 6673.

Carmichael, H.: 1964, In: Hess, W.N. (ed.) *AAS-NASA Symposium on the Physics of Solar Flares*, NASA, Washington, 451.
Chae, J.: 1999, *J. Korean Astron. Soc.* **32**, 137.
Chae, J.: 2001, *Astrophys. J.* **560**, L95.
Choe, G.S., Cheng, C.Z.: 2000, *Astrophys. J.* **541**, 449.
Dasso, S., Mandrini, C.H., Démoulin, P., Farrugia, C.J.: 2003, *J. Geophys. Res.* **108**(10), SSH 3,1.
Dasso, S., Mandrini, C.H., Démoulin, P., Luoni, M.L., Gulisano, A.M.: 2005a, *Adv. Space Res.* **35**, 711.
Dasso, S., Mandrini, C.H., Luoni, M.L., Gulisano, A.M., Nakwacki, M.S., Pohjolainen, S., van Driel-Gesztelyi, L., Démoulin, P.: 2005b, In: Fleck, B., Zurbuchen, T. (eds.) *Solar Wind 11/SOHO 16, Connecting Sun and Heliosphere*, 605.
Dasso, S., Nakwacki, M., Démoulin, P., Mandrini, C.H.: 2007, *Solar Phys.* (this issue).
Démoulin, P.: 2006, *Adv. Space Res.* **37**, 1269.
Démoulin, P., Berger, M.A.: 2003, *Solar Phys.* **215**, 203.
Feldman, W.C., Asbridge, J.R., Bame, S.J., Montgomery, M.D., Gary, S.P.: 1975, *J. Geophys. Res.* **80**, 4181.
Fletcher, L., Pollock, J.A., Potts, H.E.: 2004, *Solar Phys.* **222**, 279.
Fletcher, L., Metcalf, T.R., Alexander, D., Brown, D.S., Ryder, L.A.: 2001, *Astrophys. J.* **554**, 451.
Forbes, T.G., Priest, E.R.: 1984, In: Butler, D., Papadopoulos, K. (eds.) *Solar Terrestrial Physics: Present and Future*, NASA, Washington, 35.
Gosling, J.T.: 1990, In: Russel, C.T., Priest, E.R., Lee, L.C. (eds.) *Physics of Magnetic Flux Ropes*, *Geophys. Monogr.* **58**, AGU, Washington, 343.
Gosling, J.T., Baker, D.N., Bame, S.J., Feldman, W.C., Zwickl, R.D., Smith, E.J.: 1987, *J. Geophys. Res.* **92**, 8519.
Gosling, J.T., Birn, J., Hesse, M.: 1995, *Geophys. Res. Lett.* **22**, 869.
Greene, J.M.: 1988, *J. Geophys. Res.* **93**(A8), 8583.
Gulisano, A.M., Dasso, S., Mandrini, C.H., Démoulin, P.: 2005, *J. Atmos. Solar Terr. Phys.* **67**, 1761.
Handy, B.N., Acton, L.W., Kankelborg, C.C., Wolfson, C.J., Akin, D.J., Bruner, M.E., Caravalho, R., Catura, R.C., Chevalier, R., Duncan, D.W., Edwards, C.G., Feinstein, C.N., Freeland, S.L., Friedlaender, F.M., Hoffmann, C.H., Hurlburt, N.E., Jurcevich, B.K., Katz, N.L., Kelly, G.A., Lemen, J.R., Levay, M., Lindgren, R.W., Mathur, D.P., Meyer, S.B., Morrison, S.J., Morrison, M.D., Nightingale, R.W., Pope, T.P., Rehse, R.A., Schrijver, C.J., Shine, R.A., Shing, L., Strong, K.T., Tarbell, T.D., Title, A.M., Torgerson, D.D., Golub, L., Bookbinder, J.A., Caldwell, D., Cheimets, P.N., Davis, W.N., Deluca, E.E., McMullen, R.A., Warren, H.P., Amato, D., Fisher, R., Maldonado, H., Parkinson, C.: 1999, *Solar Phys.* **187**, 229.
Harra, L.K., Crooker, N.U., Mandrini, C.H., van Driel-Gesztelyi, L., Dasso, S., Wang, J., Elliott, H., Attrill, G., Jackson, B.V., Bisi, M.M.: 2007, *Solar Phys.* (this issue).
Hesse, M., Schindler, K.: 1988, *J. Geophys. Res.* **93**(A6), 5559.
Hirayama, T.: 1974, *Solar Phys.* **34**, 323.
Hood, A.W., Priest, E.R.: 1979, *Solar Phys.* **64**, 303.
Hornig, G., Schindler, K.: 1996, *Phys. Plasmas* **3**, 781.
Howard, R.F., Gilman, P.A., Gilman, P.I.: 1984, *Astrophys. J.* **283**, 373.
Hu, Q., Sonnerup, B.U.Ö.: 2002, *J. Geophys. Res.* **107**, SSH 10.
Jackson, J.D.: 1975, *Classical Electrodynamics*, Wiley, New York.
Klimchuk, J.A., Sturrock, P.A., Yang, W.-H.: 1988, *Astrophys. J.* **335**, 456.
Kopp, R.A., Pneuman, G.W.: 1976, *Solar Phys.* **50**, 85.
Lau, Y.-T., Finn, J.M.: 1990, *Astrophys. J.* **350**, 672.
Leamon, R.J., Canfield, R.C., Jones, S.L., Lambkin, K., Lundberg, B.J., Pevtsov, A.A.: 2004, *J. Geophys. Res.* **109**, 5106.
Lepping, R.P., Burlaga, L.F., Jones, J.A.: 1990, *J. Geophys. Res.* **95**, 11957.
Lepping, R.P., Acuna, M.H., Burlaga, L.F., Farrell, W.M., Slavin, J.A., Schatten, K.H., Mariani, F., Ness, N.F., Neubauer, F.M., Whang, Y.C., Byrnes, J.B., Kennon, R.S., Panetta, P.V., Scheifele, J., Worley, E.M.: 1995, *Space Sci. Rev.* **71**, 207.
Longcope, D.: 2005, *Liv. Rev. Solar Phys.* **2** (online article).
Longcope, D.W.: 1996, *Solar Phys.* **169**, 91.
Longcope, D.W.: 2001, *Phys. Plasmas* **8**, 5277.
Longcope, D.W., Klapper, I.: 2002, *Astrophys. J.* **579**, 468.
Longcope, D.W., Magara, T.: 2004, *Astrophys. J.* **608**, 1106.
Longcope, D.W., Silva, A.V.R.: 1998, *Solar Phys.* **179**, 349.
Longcope, D.W., Ravindra, B., Barnes, G.: 2007, *Astrophys. J.* (in press).
Longcope, D.W., McKenzie, D., Cirtain, J., Scott, J.: 2005, *Astrophys. J.* **630**, 596.
Lundquist, S.: 1950, *Ark. Fys.* **2**, 361.
Luoni, M.L., Mandrini, C.H., Dasso, S., van Driel-Gesztelyi, L., Démoulin, P.: 2005, *J. Atmos. Solar Terr. Phys.* **67**, 1734.

Mandrini, C.H., Pohjolainen, S., Dasso, S., Green, L.M., Démoulin, P., van Driel-Gesztelyi, L., Copperwheat, C., Foley, C.: 2005, *Astron. Astrophys.* **434**, 725.
Marubashi, K.: 1997, In: Crooker, N., Joselyn, J., Feynman, J. (eds.) *Coronal Mass Ejectsions*, *Geophys. Monogr.* **99**, AGU, Washington, 147.
McAllister, A.H., Martin, S.F., Crooker, N.U., Lepping, R.P., Fitzenreiter, R.J.: 2001, *J. Geophys. Res.* **106**, 29, 185.
Mikic, Z., Barnes, D.C., Schnack, D.D.: 1988, *Astrophys. J.* **328**, 830.
Nightingale, R.W.: 2000, private communications.
November, L.J., Simon, G.W.: 1988, *Astrophys. J.* **333**, 427.
Pneuman, G.W.: 1983, *Solar Phys.* **88**, 219.
Poletto, G., Kopp, R.A.: 1986, In: Neidig, D.F. (ed.) *The Lower Atmospheres of Solar Flares*, National Solar Observatory, Tucson, 453.
Priest, E.R., Hornig, G., Pontin, D.I.: 2003, *J. Geophys. Res.* **108**, 6.
Qiu, J., Ding, M.D., Wang, H., Denker, C., Goode, P.R.: 2000, *Astrophys. J.* **544**, L157.
Qiu, J., Lee, J., Gary, D.E., Wang, H.: 2002, *Astrophys. J.* **565**, 1335.
Scherrer, P.H., Bogart, R.S., Bush, R.I., Hoeksema, J.T., Kosovichev, A.G., Schou, J., Rosenberg, W., Springer, L., Tarbell, T.D., Title, A., Wolfson, C.J., Zayer, I., MDI Engineering Team: 1995, *Solar Phys.* **162**, 129.
Sturrock, P.A.: 1968, In: *IAU Symp. 35: Structure and Development of Solar Active Regions*, 471.
Sweet, P.A., 1958, In: Lehnert, B. (ed.) *Electromagnetic Phenomena in Cosmical Physics*, Cambridge University Press, Cambridge, 123.
van Ballegooijen, A.A., Martens, P.C.H.: 1989, *Astrophys. J.* **343**, 971.
Warren, H.P., Antiochos, S.K.: 2004, *Astrophys. J.* **611**, L49.
Webb, D.F., Lepping, R.P., Burlaga, L.F., DeForest, C.E., Larson, D.E., Martin, S.F., Plunkett, S.P., Rust, D.M.: 2000, *J. Geophys. Res.* **105**, 27, 251.
Welsch, B., Longcope, D.: 2003, *Astrophys. J.* **588**, 620.
Wright, A.N., Berger, M.A.: 1989, *J. Geophys. Res.* **94**(A2), 1295.